*Scientific and Technological Alliance for Guaranteeing the European Excellence in Concentrating Solar Thermal Energy*


**FP7 Grant Agreement number:** **609837**
**Start date of project:** **01/02/2014**
**Duration of project:** **48 months**

## *STAGE-STE D9.2*

# D9.2: Report on thermochemical energy storage

| | |
|---|---|
| **WP9 – Tasks 9.2** | **D9.2** |
| **Reached/Submitted:** | **August 2017** |
| **Work Package Leader:** | **PSI** |
| **Task leader:** | **PSI** |
| **Author(s):** | **Laurie André (CNRS), José Gonzalez (IMDEA), Stefan Ströhle (PSI)** |
| **Revised by:** | **Stéphane Abanades (CNRS), Manuel Romero (IMDEA), Christian Wieckert (PSI)** |
| **Document version:** | **1** |
| **Reviewed/supervised by:** | **Gilles Flamant (CNRS)** |

# Table of contents

## Abstract

Based on a thermodynamic equilibrium study to identify chemical candidate systems with the potential to be most suitable for thermochemical energy storage for CSP, cobalt oxide and manganese oxide endothermal/exothermal redox systems are selected for closer investigation. The potential improvement of their performance due to the addition of iron oxide is studied with thermogravimetric analyses methods. Fe addition is found to decrease the redox activity and energy storage capacity of $Co_3O_4$/CoO, whereas the reaction rate, reversibility and cycling stability of $Mn_2O_3$/$Mn_3O_4$ are significantly enhanced with added Fe amounts above ~15 mol%, and the energy storage capacity is slightly improved. Furthermore the performance of Ba and/or Sr perovskites for thermochemical energy storage is investigated. As good candidates Sr-Fe and Sr-Co and even better Ba-Fe and Ba-Co perovskites were identified, while Sr-Mn and Ba-Mn perovskites are not suitable. Using both, Sr and Ba (namely Sr-Ba-Co and Sr-Ba-Fe perovskites), results in an additional positive effect. A case study on the integration of a manganese oxide based thermochemical energy storage system into a CSP plant leads to the conclusion that a thermochemical storage reactor should be designed in such a way that it can be integrated with the power block in a parallel configuration rather than a serial configuration.

# 1. Introduction

A viable way to manage the inherently intermittent availability of solar energy in concentrated solar power plants is to store solar energy during on-sun hours to be able to use it later during off-sun hours, enabling on-demand electricity delivery. Thermochemical heat storage systems present some noteworthy advantages when compared with latent and sensible heat storage, namely (i) high energy storage density because the storage capacity by unit of mass or volume corresponding to the reaction enthalpy is generally high, (ii) heat storage at room temperature and long term energy storage because the products can be cooled and stored at room temperature without energy losses as heat can be stored indefinitely in chemical bonds, (iii) facility of transport because solid materials can be transferred over long distances, (iv) constant restitution temperature providing constant heat source because exothermic reactions are carried out at sufficiently high temperatures to generate electricity in constant conditions and therefore to produce a constant power.

Consequently, in the frame of STAGE-STE, potential thermochemical energy storage systems were studied in order to develop alternatives to sensible and latent thermal energy storage systems. The study first began by a literature survey coupled with an analysis of thermodynamic chemical equilibrium, which served as a primary selection of potential candidates for thermochemical energy storage. Among the candidate systems, metal oxides are convenient to work with air in an open loop since the reacting gas is $O_2$. Redox reactions based on metal oxides were studied at $pO_2$ = 0.2 atm in order to mimic air atmosphere. The improvement of redox performances for manganese oxide and cobalt oxide was studied through the synthesis of mixed metal oxides (addition of Fe). The perovskite structure is also interesting for enhanced oxygen exchange capacity, thus the redox behavior and reaction reversibility of several Ba and Sr-based formulations were studied for thermochemical energy storage application. Finally, the integration of a TCS system in a solar power plant is investigated by comparing two solid-gas reactor options, fixed and fluidized beds, and by studying parallel and serial configurations of storage unit and power block.

## 2. Selection of suitable thermochemical systems (CNRS) [1]

The selection of interesting thermochemical energy storage candidates is done regarding their compatibility with CSP plants and suitability with a set of criteria [2-4] such as high reaction temperature (400-1200°C), complete reaction reversibility, high reaction enthalpy, fast reaction kinetics, cycling stability, high availability, low cost, non-toxicity of materials.

The theoretical transition temperatures and energy storage capacity of selected metal oxide candidates are listed in Table 1.

**Table 1. Theoretical transition temperature and energy storage capacity of selected metal compounds in 20% of reacting gas.**

| Chemicals | Transition temperature (°C) | Gravimetric energy density (kJ/kg) |
|---|---|---|
| $BaO_2/BaO$ | 775 | 432.6 |
| $Co_3O_4/Co_2O_3$ | 790 | 816.1 |
| $Mn_2O_3/Mn_3O_4$ | 820 | 190.1 |
| $CuO/Cu_2O$ | 1025 | 810.2 |
| $Fe_2O_3/Fe_3O_4$ | 1290 | 485.6 |
| $Mn_3O_4/MnO$ | 1575 | 850.6 |

Experiments showed that $Co_3O_4$ is the most suited raw material given the fast reaction kinetics and complete reaction reversibility. However, the cost and potential toxicity of cobalt oxide requires the enhancement of other alternative materials. Optimization of materials reactivity is required for the other metal oxide species by using e.g. doping strategies, controlled synthesis techniques for tailored morphology, stabilization with inert materials to alleviate sintering effects, etc.. The reaction kinetics and the thermodynamic properties of the selected materials need to be characterized, as well as their performance stability over successive cycles, in order to confirm the suitability of the chosen materials for thermal energy storage (TES) applications. Then, the design and testing of adapted solar reactor concepts will also be required to demonstrate the feasibility of materials processing in solar reactor prototypes during solar heat charging and discharging. Furthermore, raw materials were mostly addressed so far, but recent research concerning the efficiency of hybrid materials, such as mixed metal oxides and perovskites, is promising and these materials need to be explored.

## 3. Metal oxides redox reactions (CNRS [5] and IMDEA)

Various metal oxides have been studied for thermochemical heat storage applications [6] due to their high gravimetric storage density, which is important for lowering the necessary amount of reactant involved in large-scale processes. The two-step thermochemical redox reactions considered for metal oxides are as follows:

$$MO_{(ox)} + \text{Heat} \rightarrow MO_{(red)} + \tfrac{1}{2}\, O_2\,(g) \quad (1)$$

$$MO_{(red)} + \tfrac{1}{2}\, O_2\,(g) \rightarrow MO_{(ox)} + \text{Heat} \quad (2)$$

Because the amount of reacting gas greatly affects the transition temperatures of the materials, metal oxides were tested in a reduction and oxidation atmosphere of 20%$O_2$-Ar in order to observe the feasibility of a thermochemical energy storage system using air. For this study, we used thermogravimetric analysis (TGA) to investigate the redox properties and reaction reversibility of the thermochemical systems.

Equilibrium calculations were performed with the FactSage 7.0 software [7] and the FToxid database, which includes models of the thermochemical properties of the oxide phases in Fe-Co-O [8] and Fe-Mn-O [9] systems. For calculations in the Fe-Co-O system, the following solid phases were considered: the $Fe_2O_3$ compound, the cubic spinel solution $(Co_{1-x}Fe_x)_3O_4$ (C-Spin) and the monoxide solution $(Co_{1-x}Fe_x)O_{1+y}$ (Monoxide). For the Fe-Mn-O systems, four phases were considered: two spinel solutions $(Mn_{1-x}Fe_x)_3O_4$, one with cubic structure (C-Spin) and the other with tetragonal structure (T-Spin), the bixbyite solution $(Mn_{1-x}Fe_x)_2O_3$ (Bixb) and the corundum solution $(Fe_{1-x}Mn_x)_2O_3$ (Cor). Two gaseous components, $O_2$ and Ar, were taken into account, with ideal mixing properties. The total pressure was always 1 atm.

For both systems, two kinds of calculations were carried out: (i) plot of phase diagrams, (ii) system equilibrium at various compositions and temperatures, providing, for each composition and at each temperature step, the phase assemblage and the cationic distribution in each solution phases, as well as the total enthalpy of the system.

The second type of calculations gives access to the theoretical mass loss (i.e. oxygen storage capacity), Δm, as defined by (Eq. 3). This quantity is directly comparable to the mass change measured by TGA.

$$\Delta m\ (\%) = 100.\frac{mass\ of\ solid\ at\ T_{max} - mass\ of\ solid\ at\ T_{min}}{mass\ of\ solid\ at\ T_{min}} \quad (3)$$

where $T_{min}$ and $T_{max}$ are referring to the minimal and maximal temperature of the thermochemical cycle.

The enthalpy of the reduction reaction (Eq. 1), $\Delta_r H$, was calculated according to (Eq. 4). This quantity is compared to the heat of reaction determined by DSC analysis. For reactions occurring on a large temperature range, this calculation includes a contribution due to the calorific capacity of the compounds (sensible heat), which leads to an overestimation of the enthalpy strictly related to the reaction.

$$\Delta_r H(kJ/kg\ of\ s^0) = \frac{1}{m_{s^0}}\left[m_{s^1}H^{s^1}(T_{end}) + m_{s^2}H^{s^2}(T_{end}) + m_{O2}H^{O2}(T_{end})\right] - H^{s^0}(T_{beg}) \quad (4)$$

where $T_{end}$ is the temperature (°C) at the end of the phase transition or the maximal temperature of the cycle; $T_{beg}$ is the temperature (°C) at the beginning of the phase transition; $m_S^0$ is the mass (kg) of the solid phase at $T_{min}$; $m_S^1$ and $m_S^2$ are the mass (kg) of the solid phases at $T_{end}$; $m_{O2}$ is the mass (kg) of dioxygen at $T_{end}$; $H^x(T)$ is the enthalpy (kJ/kg) of the compound x at the temperature T.

## 3.1. Cobalt oxide (CNRS)

Most research focusing on metal oxides is considering cobalt oxide as a promising thermochemical energy storage material. The reduction temperature of $CO_3O_4$ to CoO in air atmosphere is estimated to be between 880 and 930°C according to the scientific literature [10-13]. Cobalt oxide was tested as heat storage material in the form of powder [10], foam [11,12] and pellets [13]. While Karagiannakis *et al.* (2014) [13] obtained the highest measured energy density of 515 kJ/kg for the pellet and state that the structured material exhibits better heat transfer than powder, Agrafiotis *et al.* (2015) [11, 12] noticed the presence of cracks appearing in pellets after a few cycles while foams showed better mechanical stability. The addition of a secondary metal oxide can be a way to modify the properties of a pure oxide. The cyclability and transition temperature of cobalt oxide was tested after the addition of various secondary oxides and Block *et al.* (2014) [14] reported that both addition of iron oxide to cobalt oxide or addition of cobalt oxide to iron oxide reduces the enthalpies of reaction compared to those of the pure oxides. However, they estimated that 10% iron oxide doped cobalt oxide is still showing high enthalpy of reaction and possesses higher reduction/oxidation reversibility than pure cobalt oxide. This phenomenon is being investigated here by the synthesis and analysis of mixed Co-Fe oxide systems.

The calculated Co-Fe-O phase diagram for $pO_2$ = 0.20 atm is presented in Fig. 1a. It shows that, at equilibrium, the iron content greatly influences the composition and the amount of the monoxide phase formed at 1050°C when heating the spinel phase from 800°C. For small Fe additions ($0 < x(Fe) < 0.1$), the spinel phase is fully converted into the monoxide phase. At very high Fe content ($x(Fe) > 0.6$), there is no phase transition achievable below 1200°C, which is the upper temperature limit usually considered for TES applications. For intermediate Fe content ($0.1 < x(Fe) < 0.6$), an increasing proportion of spinel phase is not converted into monoxide. As an example, Fig. 1b presents the influence of the temperature on the phases amount for x(Fe)= 0.25. A temperature of about 1460°C is required to fully convert the spinel phase into the monoxide phase. Furthermore, as illustrated in Fig. 1c for x(Fe)= 0.25, the monoxide phase $(Co_{1-x}Fe_x)O_{1+y}$ presents a noticeable over-stoichiometry (y) in oxygen, which increases with temperature.

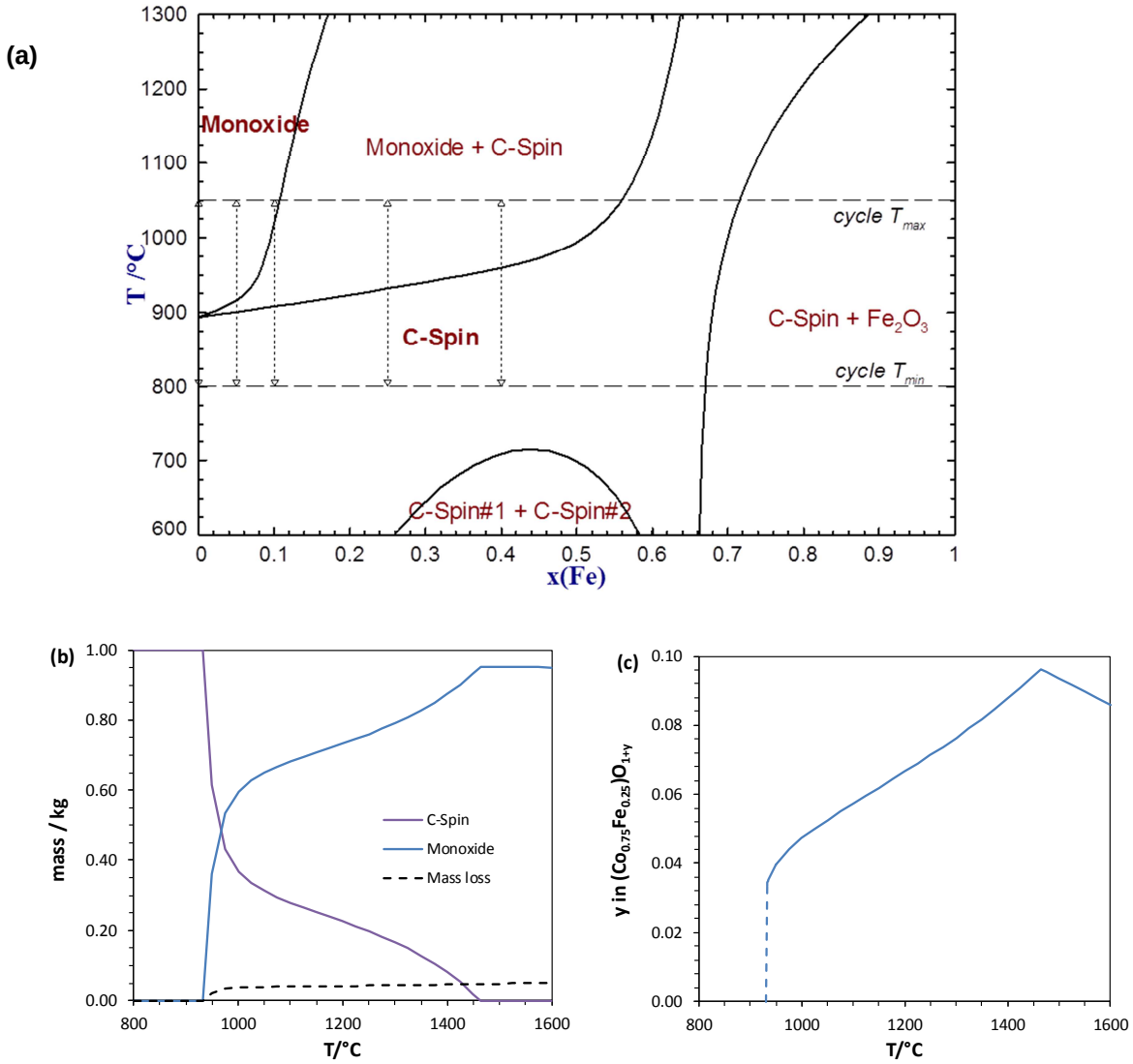


***Figure 1.*** *(a) Calculated Co-Fe-O phase diagram at $pO_2$ = 0.20 atm, (b) calculated temperature evolution of the mass of solid phases for x(Fe) = 0.25, (c) calculated temperature evolution of oxygen over-stoichiometry (y) in the monoxide phase $(Co_{0.75}Fe_{0.25})O_{1+y}$.*

The TGAs of cobalt-based oxides are presented in Figs. 2 and 3 with different temperature programs. A first observation is that a noticeable change in the re-oxidation onset temperature is measured between the samples with 0 to 10 mol% Fe (Fig. 2b-c, 3c-e) and with 25 to 40 mol% Fe (Fig. 2a, 3a-b). Indeed, the re-oxidation step starts at the beginning of the temperature decrease (i.e. 1050°C) for the samples containing 25 mol% Fe and 40 mol% Fe, which is in line with the phase diagram (Fig. 1a) since the two-phase equilibrium strongly depends on the temperature. The Co-Fe samples were kept in a reduced state after TGA (final cooling step in Ar to avoid re-oxidation in Fig. 3). Phase identification confirmed the presence of the single monoxide phase for low Fe contents (0 and 5 mol%), whereas the samples consisted of a mixture of monoxide and spinel phases for higher Fe contents (10-40 mol%), in agreement with the calculated phase diagram.

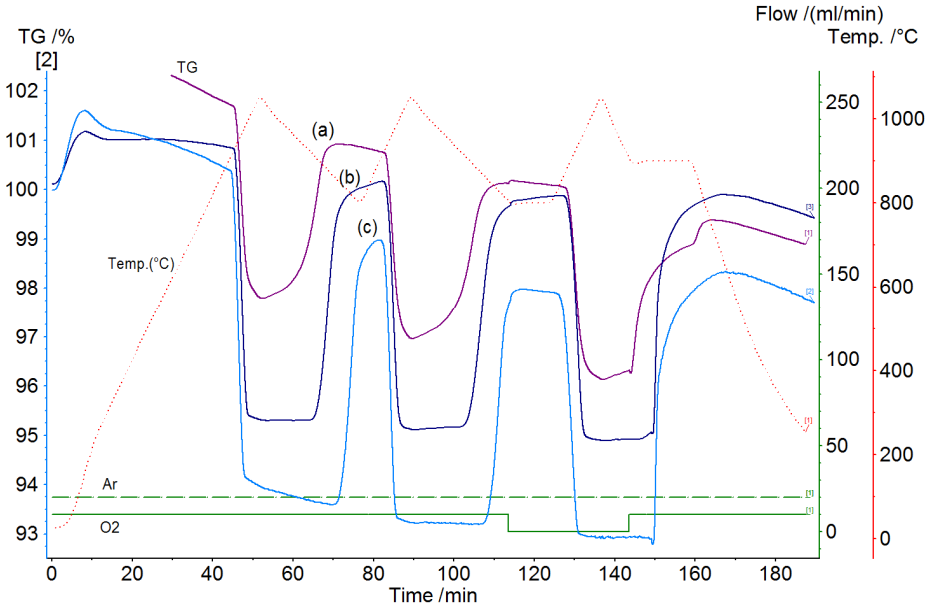


***Figure 2.*** *TGA of $Co_3O_4$/CoO with addition of (a) 25 mol% Fe, (b) 10 mol% Fe, (c) 5 mol% Fe, including a final re-oxidation step under 20% $O_2$/Ar at the end.*

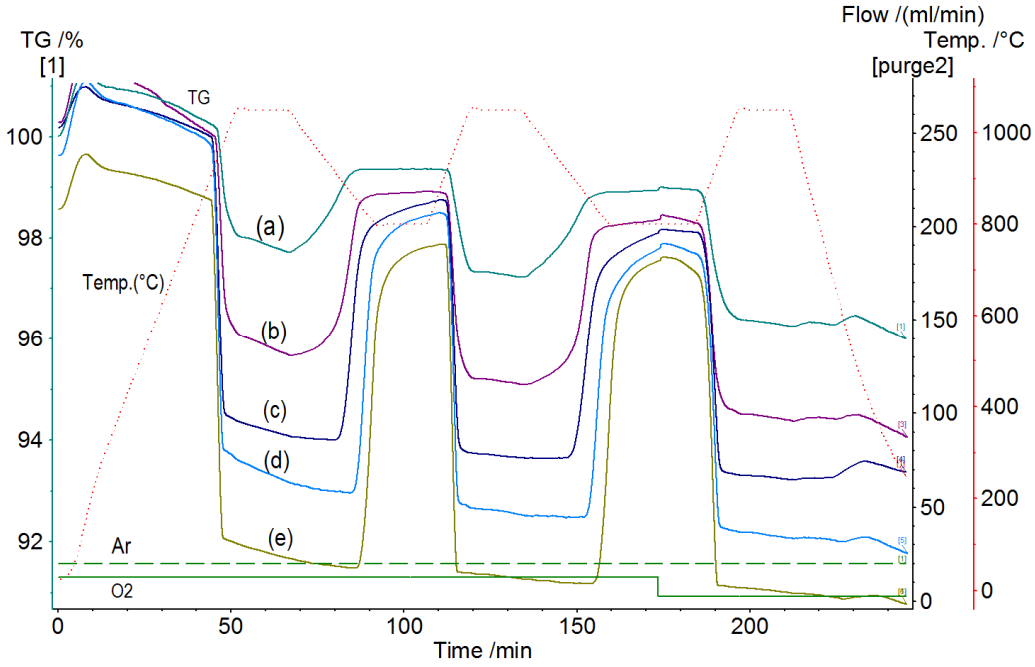


***Figure 3.*** *TGA of $Co_3O_4$/CoO with addition of (a) 40 mol% Fe, (b) 25 mol% Fe, (c) 10 mol% Fe, (d) 5 mol% Fe, (e) no Fe added, ending on a final reduction step under Ar.*

The influence of Fe incorporation on reaction temperatures is reported in Fig. 4. The temperatures at peak reaction rate (i.e. temperatures at which the reaction kinetics reached its maximum, Fig. 4) were measured. A gradual increase of the reduction and oxidation temperatures is observed with increasing amount of iron in the material, which is consistent with the phase diagram (Fig. 1a). An effect of Fe addition on the temperature gap between reduction and oxidation is also evidenced. Indeed, as both temperatures rise with Fe addition, it can be noticed that the gap between the reduction and oxidation temperatures reduces. For

40 mol% Fe, the onset temperature for reduction has increased by 50°C compared to pure $Co_3O_4$, while the onset temperature for oxidation has increased by 90°C. The reduction of this temperature gap is an asset for large-scale applications since it reduces the amount of energy spent for the heating and cooling of the system between the charge and the discharge steps. However, an increase in the oxidation temperature may also be a disadvantage if the system must be externally heated to initiate the oxidation (in case the material is stored in reduced form at room temperature).

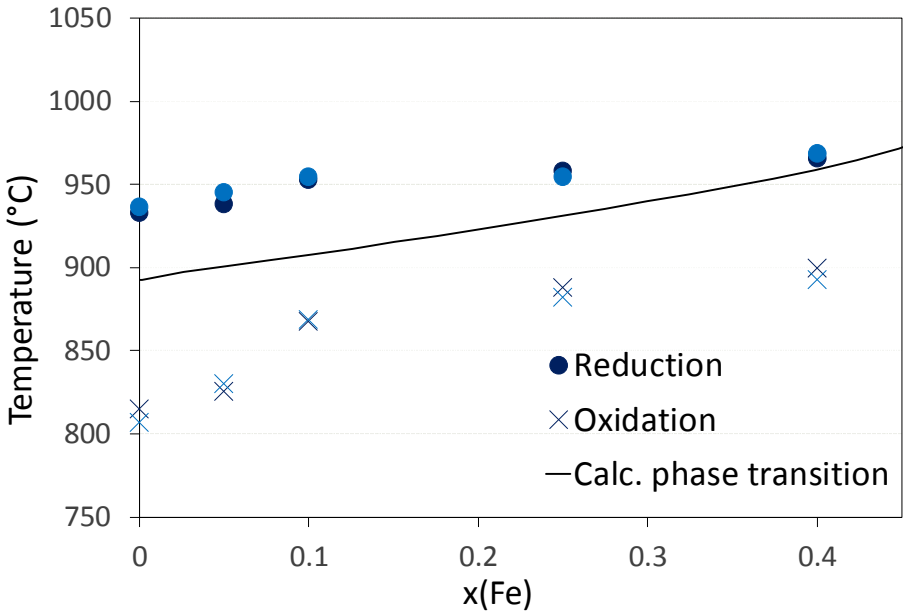


***Figure 4.*** *Experimental temperatures at peak reaction rate for cobalt-based oxides in 20%$O_2$/Ar and comparison with the calculated temperature of the C-Spin/Monoxide transition.*

Fig. 5 shows, along with the calculated equilibrium values, the maximum values of Δm measured for each oxide composition, which means the highest amount of $O_2$ released during reduction, and the average Δm for the three redox cycles. The hypothetic case of a full conversion of the initial spinel into a stoichiometric monoxide, calculated according to (Eq. 5), is also plotted in Fig. 5.

$$(Co_{1-x}Fe_x)_3O_{4(s)} = 3\ (Co_{1-x}Fe_x)O_{(s)} + 0.5\ O_2(g) \quad (5)$$

Measurements of the Δm values clearly show that increasing the amount of iron in the material reduces the amount of $O_2$ it is able to release at a given temperature. Furthermore, the maximum Δm values are in excellent accordance with equilibrium calculations, which implies that a full conversion has been reached.

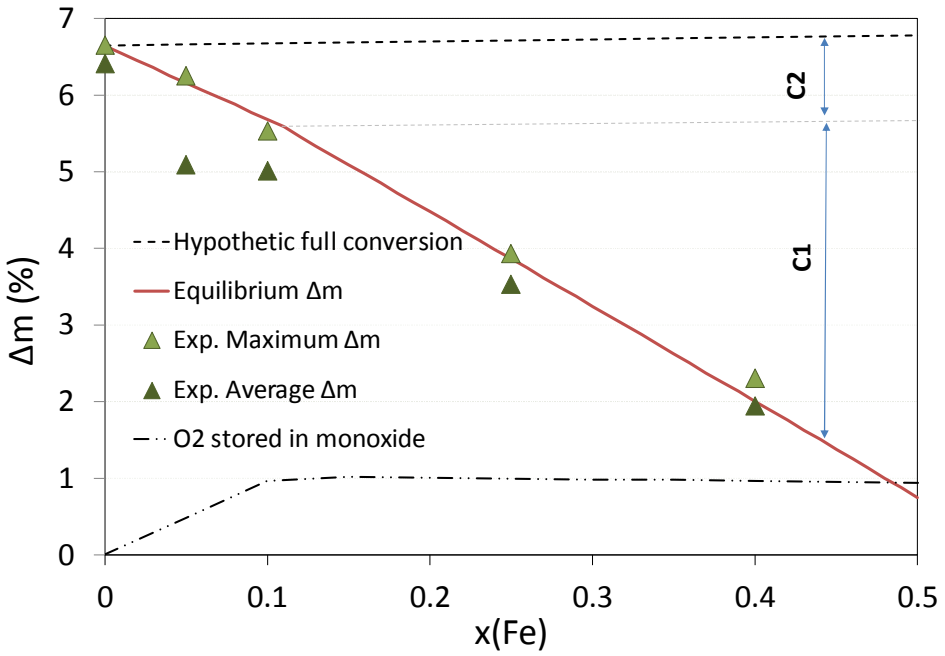


***Figure 5.*** *Average and maximal experimental mass loss (Δm in %) of the Co-Fe mixed oxide between 800°C and 1050°C compared to Δm at thermodynamic equilibrium.*

According to the thermodynamic model, the decrease in $O_2$ storage capacity with increasing Fe content is due to a combination of two factors. First, as evidenced by the phase diagram and the temperature profile for x(Fe) = 0.25 (Fig. 1b), the upper temperature limit of 1050°C does not lead to a full conversion of the spinel phase when x(Fe) > 0.10. This contribution is represented as C1 in Fig. 5. It does not account for the decrease in Δm evidenced for x(Fe) = 0.05 and 0.10 (C2 in Fig. 5), which should be closer to the mass loss calculated according to (Eq. 5) since a full conversion into monoxide occurs. The second factor is linked with the fact that the monoxide solid solution becomes non stoichiometric with the incorporation of Fe (Fig. 1c). This leads to a residual storage of oxygen in the monoxide phase, according to (Eq. 6):

$$(Co_{1-x}Fe_x)_3O_{4(s)} = 3\,(Co_{1-x}Fe_x)O_{1+y(s)} + (1-3y)/2\;O_2(g) \qquad (6)$$

where y is the over-stoichiometry of oxygen in the monoxide phase.

As illustrated in Fig. 5, the calculated contribution of the oxygen over-stoichiometry in the monoxide phase at 1050°C accounts for a loss of storage capacity of about 1% per unit mass of spinel when x(Fe) > 0.10, as compared to a maximum capacity of 6.6% for pure cobalt oxide.

As for the cycling stability, for pure $Co_3O_4$, the average Δm is the same as both the theoretical value and the maximum value measured experimentally. This means that the amount of $O_2$ released and regained did not change, confirming the good material cycling stability over three cycles, as already reported by several authors [11-16]. For the samples containing 5 and 10 mol% iron, since the average Δm falls slightly below the theoretical and maximum value, a minor loss in $O_2$ exchange capacity upon cycling is evidenced. Conversely, the amount of $O_2$ exchanged remains stable over cycles for larger Fe contents (x(Fe) > 0.10) at the expense of a decreased oxygen storage capacity. Thus, the cycling stability of cobalt oxide does not suffer

from the addition of iron, as the re-oxidation conversion rate is not significantly decreasing over multiple cycles for Co-Fe mixed oxides, similarly to pure $Co_3O_4$.

Regarding the effect of the gas flow composition, the measured Δm due to the reduction under pure Ar was not significantly different from the one measured with 20% $O_2$/80% Ar. However, the reduction onset temperature under Ar was decreased by 60 to 80°C, to reach a value of about 860°C, almost independent of x(Fe). These data are rather different from the equilibrium state calculated with the thermodynamic model. Indeed, under pure Ar, the experimental oxygen partial pressure should be around $10^{-5}$ atm (10 ppm $O_2$), which corresponds to a transition temperature of about 650-700°C but it increases with a higher $pO_2$. Furthermore, the calculated transition temperature depends noticeably on the composition of the system. It is thus concluded that, with a heating rate of 20°C/min, the system does not reach equilibrium at low temperature, most likely because of solid-state diffusion limitations. Independently of the system composition, a minimum temperature threshold of about 850°C is required to achieve the phase transition.

The effect of applying a higher temperature limit than 1050°C was also estimated, both with experimental measurements and calculations. Cycles with a maximal temperature of 1150°C were carried out on $Co_3O_4$ with 5 mol% Fe. While this sample behaved well with a maximum temperature set at 1050°C, the heating up to 1150°C clearly affected its reactivity. Indeed, the sample did not regain the whole mass on cooling (67% average instead of 86% when heating at 1050°C) and was sintered at the end of the run.

Furthermore, equilibrium calculations show that applying a temperature limit higher than 1050°C will not increase drastically the oxygen storage capacity of mixed Co-Fe oxides, as illustrated by Fig. 6. Indeed, for Fe contents between 0 and 10 %, the oxygen storage capacity is almost constant with temperature, because the non-stoichiometry of the monoxide is stable. For higher Fe contents ($0.10 < x(Fe) < 0.40$), a small increase of the storage capacity is evidenced at high temperature, due to a higher conversion rate of the spinel phase (Fig. 1b), but Fe addition is still detrimental for the total storage capacity.

As reported in Fig. 7, the measured reaction enthalpies are decreasing with increasing amount of Fe: the highest measured enthalpy is 597 kJ/kg for pure $Co_3O_4$, while the lowest is 50.7 kJ/kg for $x(Fe) = 0.40$. It should be noted that the DSC peaks for $x(Fe) = 0.40$ are very small, which makes them difficult to analyze. For pure $Co_3O_4$, our data is close to the value of 576 kJ/kg obtained by [14] with a similar experimental procedure. As recently discussed in details by Block *et al*. [17], this kind of DSC measurements, operated in an open reactor at a rather fast heating rate, is not able to reproduce the tabulated enthalpy value, which is commonly reported as 844 kJ/kg [11-12,15-16]. To explain the large discrepancy, the authors state that the contribution of a $Co^{3+}$ spin-state change, associated with an enthalpy of about 222 kJ/kg, is not measured by dynamic techniques.

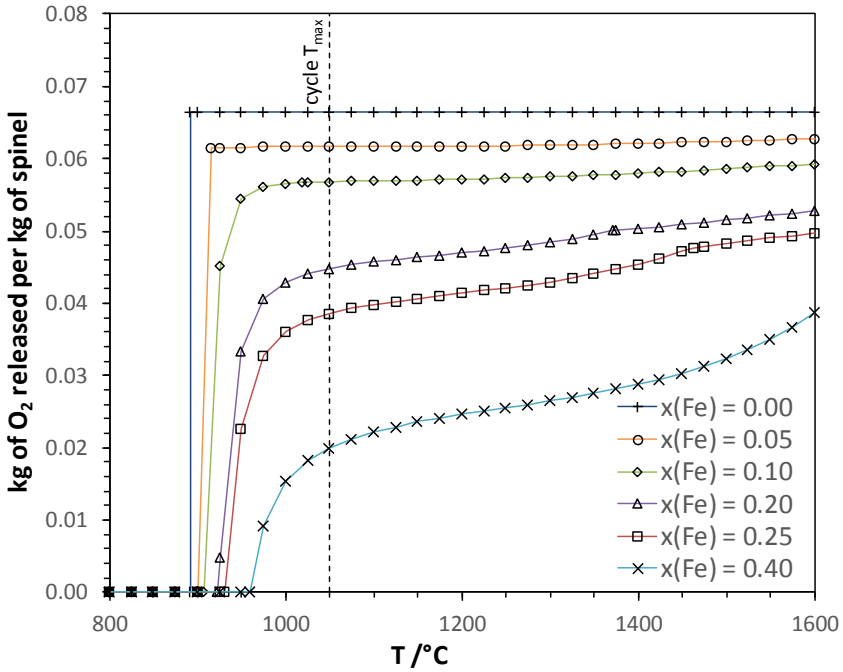


***Figure 6.*** *Temperature evolution of the amount (kg) of $O_2$(g) released per kg of cobalt-based spinel containing various amounts of Fe.*

The thermodynamic model used in this study [8], which takes into account the heat capacity anomaly due to spin-state transition of $Co^{3+}$, leads to an enthalpy of reaction of 749 kJ/kg for x(Fe) = 0. This is noticeably lower than the commonly admitted value of 827 kJ/mol [14, 17]. For higher Fe contents, the calculations reproduce well the general trend (decrease of $\Delta_r H$) with a systematic gap of about 180 kJ/kg.

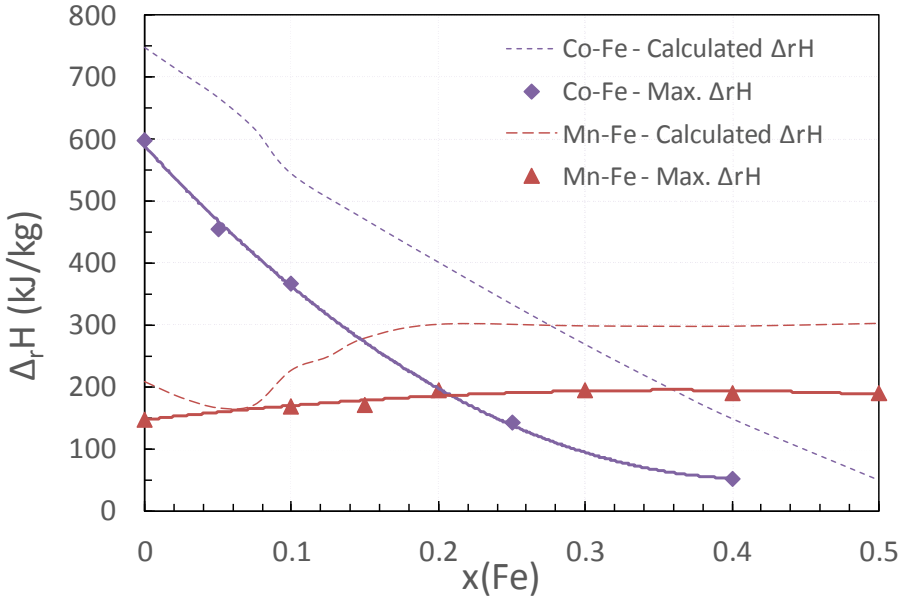


***Figure 7.*** *Experimental and calculated enthalpies of reaction for the Co-Fe and Mn-Fe mixed oxides.*

In TES applications, the enthalpy of the reaction is related to the oxygen storage capacity of the material (the energy stored/released during the reduction/oxidation is related to the reaction extent that corresponds to the quantity of $O_2$ released/captured). As evidenced by measurements and calculations, the gravimetric energy storage density of mixed oxides is decreased when compared with pure $Co_3O_4$, resulting in less storage capacity per gram of material. This observation is in accordance with the work of Block *et al.* [14], who stated that both pure $Co_3O_4$ and $Fe_2O_3$ show higher enthalpies of reaction than any mixture of the two.

In summary, while the $Co_3O_4$/CoO redox pair shows very good cycling stability, the incorporation of Fe to $Co_3O_4$ shows adverse effect on the redox performances since both the maximum amount of $O_2$ exchanged and the reaction enthalpy are lowered when the amount of iron added is increased. The increasing amount of iron added to $Co_3O_4$ reduces the maximum oxygen exchange capacity during a redox cycle. According to equilibrium calculations in the Co-Fe-O system, the addition of iron to $Co_3O_4$ results in a lower amount of $O_2$ exchanged during cycles and a loss of the reduction reaction enthalpy, due to an incomplete conversion of the spinel phase at 1050°C and to the formation of a non-stoichiometric monoxide. The addition of iron also increases the reduction and oxidation temperatures, while slightly decreasing the gap in temperature between the reduction and the oxidation step.

## 3.2. Manganese oxide (CNRS and IMDEA)

Manganese compounds are excellent candidates as heat storage material due to their excellent characteristics (low cost, environmentally friendly, reaction temperature etc.). The Mn-O system is rather complex with various stable crystalline phases ($MnO_2$, $Mn_2O_3$, $Mn_3O_4$ and MnO) depending on the temperature and oxygen partial pressure.

### CNRS contribution

Concerning the $Mn_2O_3$/$Mn_3O_4$ couple, the reduction step of manganese oxide was observed in the range of 920-1000°C and the notably slow re-oxidation was observed in the range of 850-500°C with a gravimetric energy storage density of 110 kJ/kg. It is specified that the re-oxidation happens in two steps, the first one being during the cooling and in between 700°C-500°C and the second one being during the re-heating and in the range of 500-850°C [13]. As $Mn_2O_3$/$Mn_3O_4$ is a promising metal oxide redox pair for thermochemical heat storage, Carillo *et al*. (2014) [18] tested the durability of this material over thirty oxidation-reduction cycles performed by thermogravimetry. They enlightened the necessity to pay attention to the initial particle size of these oxides since it influences the kinetics and the thermodynamics of the reaction. Especially, smaller particles would contribute in lowering the oxidation temperature, but it would also hinder the diffusion of $O_2$ by favoring the sintering of the material. Based on these results, the influence of the morphology of the material on its reactivity is currently under investigation by considering different synthesis techniques (Figure 8).

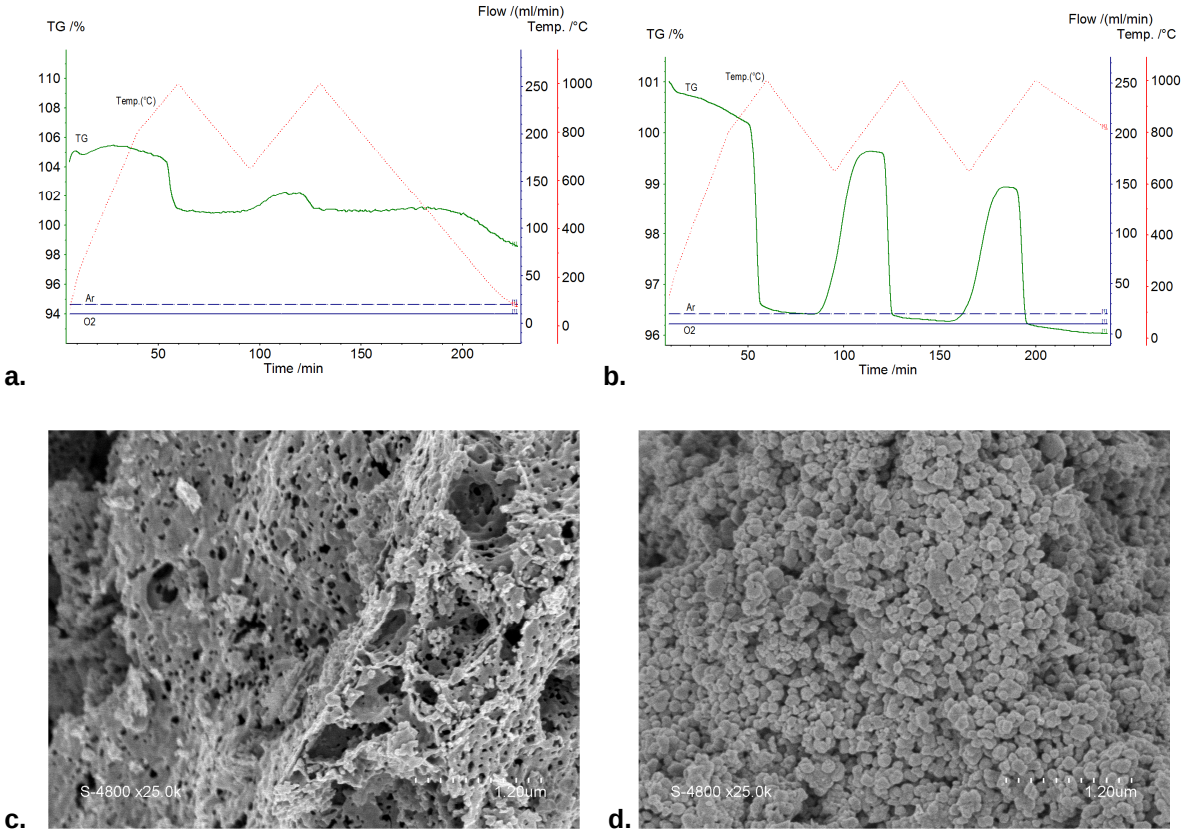


***Figure 8.*** *TGA of a. porous $Mn_2O_3$ and b. nanometer sized particles $Mn_2O_3$, SEM of c. porous $Mn_2O_3$ and d. nanometer sized particles $Mn_2O_3$.*

Carillo *et al*. (2015) [19] further studied the performances of manganese oxide for thermochemical energy storage and sought to improve it with the addition of iron oxide to the material. The incorporation of iron oxide does not allow avoiding the sintering encountered with manganese oxide, however it increases the heat storage density of the material and it stabilizes and enhances its oxidation rate over an experiment of thirty redox cycles. The material presenting the fastest and the most stable oxidation reactions in their study is $Mn_2O_3$ doped with 20% Fe. Carillo *et al* (2015) [20] also considered Fe-Cu co-doping in manganese oxide in order to study its effect on the temperature gap of about 200°C between the reduction and oxidation temperatures of this material, as well as the effects on its reaction kinetics. They showed the possibility to reduce the reduction temperature with the incorporation of Cu and to increase the oxidation temperature with the incorporation of Fe. However, they also reported a lower reduction and oxidation rates with the addition of 5% Cu. In our study, the improvement of the reactivity of manganese oxide through the addition of iron oxide was investigated.

The calculated Mn-Fe-O phase diagram is presented in Fig. 9, for $pO_2$ = 0.20 atm. Again, the expected behavior of the mixed oxides is strongly dependent on the system composition. At Fe contents above 50%, the requested temperature to reach a full conversion of the initial oxide into a spinel phase is above 1100°C. At very low Fe contents ($0 < x(Fe) < 0.05$), the stable phase at 1050°C is the tetragonal spinel. For $0.05 < x(Fe) < 0.15$, the transition of bixbyite to cubic spinel goes through two consecutive two-phase zones (T-Spin+Bixb and T-

Spin+C-Spin). Finally, above about 20 mol% Fe, the material transforms almost directly from the bixbyite phase to the cubic spinel.

According to the model [9], the non-stoichiometry of the oxide phases should not play a significant role regarding oxygen storage capacity. Indeed, the bixbyite phase $(Mn_{1-x}Fe_x)_2O_3$ is considered as fully stoichiometric. For the spinel phases T-Spin and C-Spin, a cationic non-stoichiometry is considered in the model, with the presence of cationic vacancies. However, the vacancies concentration at 1050°C is at the most $1.4.10^{-4}$ mol per mol of Mn+Fe, which leads to a negligible impact on the oxygen storage capacity. In the composition range $0 < x(Fe) < 0.5$ considered in this study, the redox cycle is thus represented by:

$$(Mn_{1-x}Fe_x)_2O_3 = 2/3\ (Mn_{1-x}Fe_x)_3O_{4(s)} + 1/6\ O_2(g) \qquad (7)$$

At equilibrium, according to the model, the theoretical amount of $O_2$ exchanged between 750°C and 1050°C remains thus the same in the $0 < x(Fe) < 0.5$ composition range.

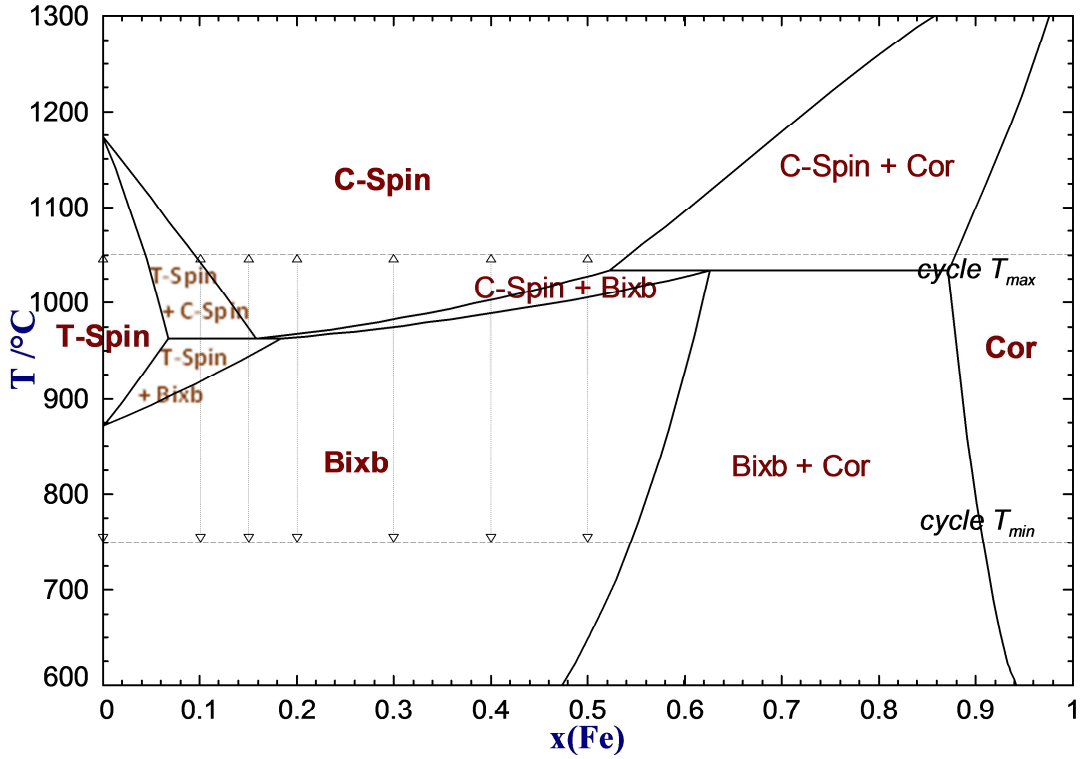


***Figure 9.*** *Calculated Mn-Fe-O phase diagram at $pO_2$ = 0.20 atm.*

The TGA, presented in Fig. 10, shows that the sample with the composition x(Fe) = 0.10 is unable to regain its full mass during oxidation, as the mass lost during the first reduction step is not recovered during the re-oxidation step, similarly to the case of pure $Mn_2O_3$. Conversely, the other compositions, from 15 mol% Fe to 50 mol% Fe, are regaining their lost mass in a complete reversible way. XRD analysis of Mn-Fe samples after TGA was performed. The XRD pattern of $Mn_2O_3$ with 10 mol% Fe is identified as a mixture of tetragonal spinel structure and $Fe_2O_3$, which confirms the poor re-oxidation yield of the cycled material. Conversely, the XRD pattern of $Mn_2O_3$ with 20, 30, 40 and 50 mol% Fe after TGA is

identified as $(Mn_{1-x}Fe_x)_2O_3$ with $Fe_2O_3$ visible on the sample with the highest amount of Fe added, which denotes the complete re-oxidation of the samples after TGA. SEM characterization of the cycled materials compared with the fresh ones reveals sintering regardless of the amount of Fe, which does not alter the cycling ability of Mn-Fe mixed oxides. Sintering is thus not the cause of the reactivity loss in the case of pure $Mn_2O_3$ and $Mn_2O_3$ mixed with 10 mol% Fe.

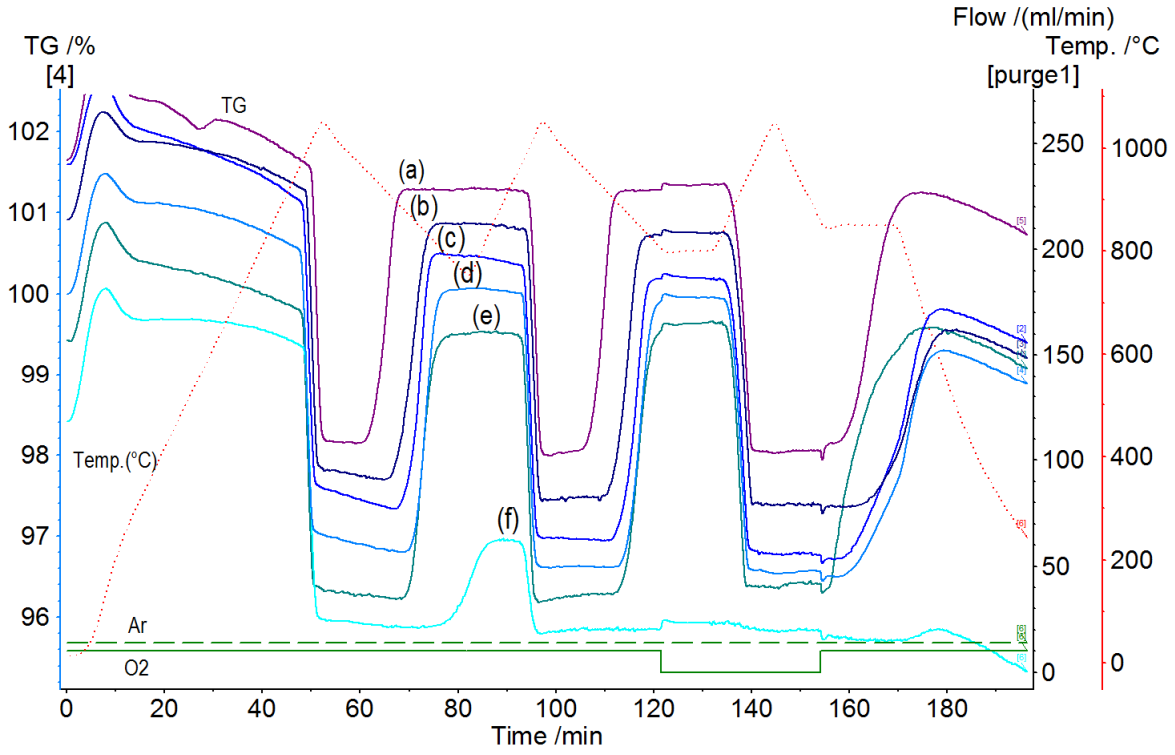


***Figure 10.*** *TGA of $Mn_2O_3/Mn_3O_4$ with addition of (a) 50 mol% Fe, (b) 40 mol% Fe, (c) 30 mol% Fe, (d) 20 mol% Fe, (e) 15 mol% Fe, and (f) 10 mol% Fe.*

Experimental and theoretical mass variations, Δm, were compared. As illustrated in Fig. 11a, all the samples feature the same Δm during the first reduction, in good accordance with the equilibrium calculations summarized by (Eq. 7). However, pure $Mn_2O_3$ shows cycling stability issues as already evidenced by [18]. This phenomenon is reflected by the drop of the experimental Δm during 2$^{nd}$ and 3$^{rd}$ cycles, showing a decrease of redox activity with redox cycling. Similarly, $Mn_2O_3$ mixed with 10 mol% Fe also loses cycling stability, regaining only 31% of its lost mass (Fig. 10f). From x(Fe) = 0.15 to 0.50, a great improvement is evidenced, since the experimental Δm value for each cycle remains close both to the maximum Δm value and to the equilibrium value, which denotes negligible deactivation during redox cycling. The addition of iron to $Mn_2O_3$ thus increases the re-oxidation yield of the material and enhances the cycling stability, as recently observed by Carrillo *et al.* [18].

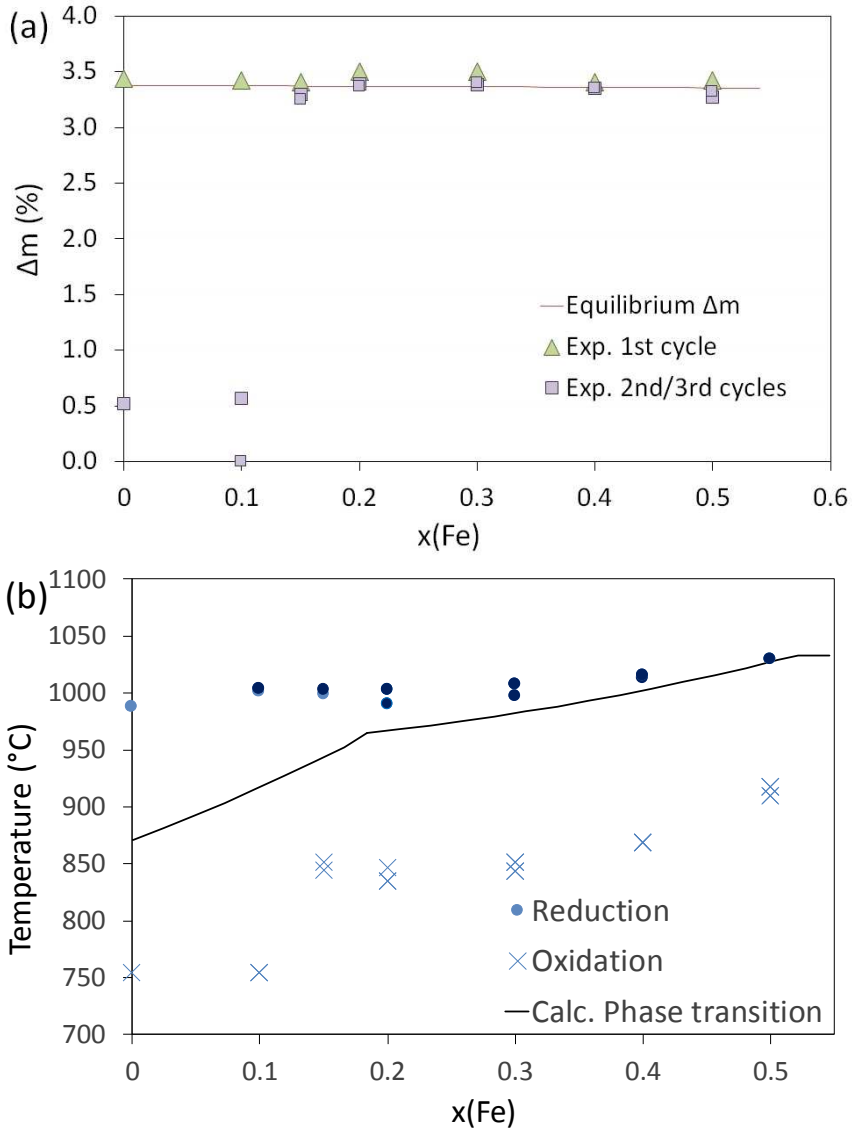


***Figure 11.*** *(a) Evolution of experimental Δm (%) during reduction compared to theoretical Δm ($pO_2$ = 0.20 atm), (b) Experimental temperatures at peak reaction rate for manganese-based oxides in 20%$O_2$/Ar and comparison with the calculated temperature of the Bixb/Spinel transition.*

Experimental measurements clearly indicate that the minimum Fe content necessary to improve the TES properties of mixed Mn-Fe oxides lies between 10 and 15 mol% Fe. The phase diagram indicates that this corresponds to the formation of the cubic spinel phase only, compared to lower Fe contents, where the tetragonal spinel cannot be reversibly oxidized during cooling. The addition of 20 mol% Fe in $Mn_2O_3$ was previously mentioned as the optimal composition for obtaining the highest enthalpy and most stable re-oxidation yields [18]. However, the authors also obtained full conversion for all their tested samples regardless of the Fe content (especially below 10% Fe), which contrasts sharply with the results of the present study in which pure $Mn_2O_3$ and $Mn_2O_3$ sample with 10 mol% Fe were not able to fully recover the $O_2$ lost mass. More recently, an in-depth kinetic and mechanistic study focused on the 20 mol% Fe composition was carried out by the same group [21]. It is stated that the cationic distribution in the spinel structures (cubic and tetragonal) might be

sufficiently different to explain the strong variation in the kinetics of the oxidation reaction. The use of the thermodynamic model proposed by Kang and Jung [9] brings support to this explanation. Indeed, as illustrated in Fig. 12a, the calculated cationic distribution evidences that the amount of $Mn^{2+}$ on octahedral sites of the spinel strongly increases in the cubic spinel. Furthermore, it has been shown that $Mn^{2+}$ on octahedral sites is easier to oxidize than $Mn^{2+}$ on tetragonal sites [22]. This difference might very well explain the reason why the cycling properties of the cubic spinel are much better than those of the tetragonal spinel.

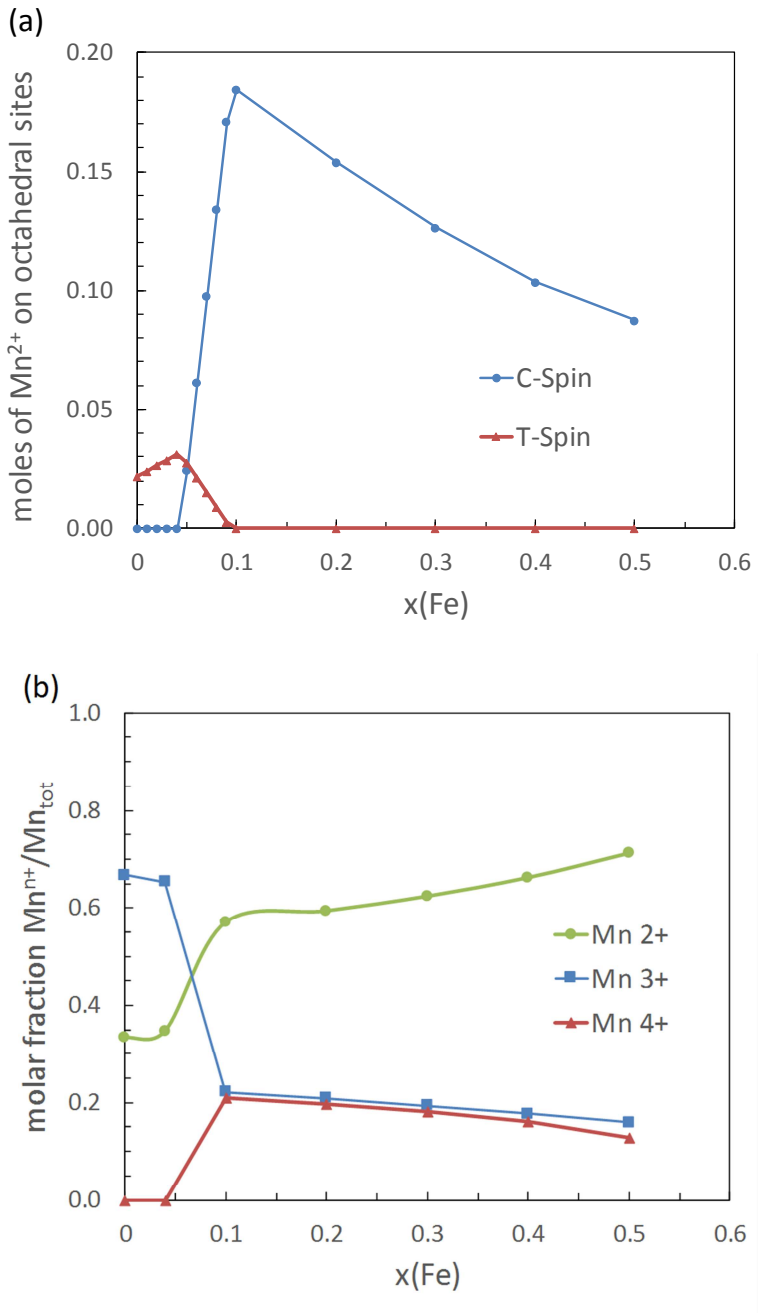


***Figure 12.*** *a) Evolution of the amount of $Mn^{2+}$ on octahedral sites of the spinel phases with Fe content, at 1050°C. b) Evolution of the oxidation number of Mn cations in the spinel phases with Fe content, at 1050°C.*

Another difference between the two spinel structures is that, in the cubic spinel, a disproportionation reaction takes place according to $Mn^{3+}$ = 1/2 $Mn^{4+}$ + 1/2 $Mn^{2+}$, as illustrated in Fig. 12b. The increased amount of $Mn^{2+}$ in the cubic spinel, which can be more easily oxidized than $Mn^{3+}$ thanks to the favored thermodynamic driving force, may also explain the enhanced re-oxidation ability of the cubic spinel. This result means that pure $Mn_2O_3$ (that reduces into pure tetragonal spinel) and mixed Mn-Fe oxides with Fe content below 15% cannot be suitable candidates for achieving reversible reactions because of the poor re-oxidation ability of the tetragonal spinel formed upon reduction.

As for the influence of Fe incorporation in $Mn_2O_3$ on the reaction temperatures, a similar tendency as with cobalt oxide is observed. The reduction and oxidation temperatures of $Mn_2O_3$ softly increase with increasing amount of added iron (Fig. 11b). According to TGA, an increase of 60°C is noted between the onset temperatures for reduction of pure $Mn_2O_3$ and $Mn_2O_3$ with 50 mol% Fe. Concomitantly, a temperature increase of 160°C is observed for oxidation of $Mn_2O_3$ with 50 mol% Fe when compared to $Mn_2O_3$ alone. This way, the reaction temperature can be tuned. On top of an increase of the reaction temperature, addition of iron also reduces the temperature gap between the reduction and the oxidation step. A temperature increase was also reported by [18], with 60°C difference between 0 and 40 mol% Fe added for the reduction, and 236°C for the oxidation.

Regarding the effect of the gaseous atmosphere composition, the experimental and theoretical $\Delta m$ values for the reduction in pure Ar atmosphere were found stable with the addition of Fe to manganese oxide and similar to the $\Delta m$ measured with 20% $O_2$. Again, the reduction temperature increases with the $O_2$ partial pressure. The onset temperature for reduction under inert atmosphere rises with the amount of Fe added to manganese oxide, from about 800°C for pure $Mn_2O_3$ up to 903°C for x(Fe) = 0.5. The phase diagram calculated at low $pO_2$ ($10^{-5}$ atm) shows that the decreasing the oxygen content results in enhancing the tetragonal spinel stability, which is likely to be detrimental to the cycling stability of the materials.

As for the energy storage density, the measured enthalpy for the first reduction step with full conversion of pure $Mn_2O_3$ (148 kJ/kg) is smaller than theoretical estimations of 190.1 kJ/kg at turning temperature ($\Delta G^o$ = 0) of 915°C [1]. An average of 187.7 kJ/kg is measured for the samples with compositions between 20 and 50 mol% Fe. Increasing the amount of Fe thus slightly improves the energy storage capacity of the material at low Fe contents while it remains unchanged above ~20 mol% Fe (Fig. 7). Accordingly, the thermodynamic calculations indicate that an increase of $\Delta_rH$ is expected when the Fe content increases from 0 mol% (207 kJ/kg) to 20 mol% (300 kJ/kg), and is stable for higher Fe contents.

In summary, the addition of iron to manganese oxide enhances considerably the cycling stability of the material by improving the re-oxidation yield thanks to the formation of a reactive cubic spinel phase. Also, the higher the amount of Fe added to $Mn_2O_3$, the higher the reaction temperatures. In addition, the gap in temperature between the reduction and the oxidation decreases with higher iron content. The low re-oxidation yield observed for pure $Mn_2O_3$ and $Mn_2O_3$ with 10 mol% Fe is attributed to the low reactivity of the tetragonal spinel phase. The addition of Fe to $Mn_2O_3$ becomes effective for the enhancement of the cycling stability above ~15 mol% Fe, with the suppression of any transition involving this tetragonal

spinel phase. The markedly improved reactivity of the cubic spinel featuring reversible reactions is attributed to the increased amount of $Mn^{2+}$ cations (resulting from $Mn^{3+}$ disproportionation) on octahedral sites of the spinel.

The addition of Fe to $Mn_2O_3$ was shown to be beneficial to tune the temperature of redox reactions, to reduce the gap in temperature hysteresis between the reduction and the oxidation step, as well as to enhance the re-oxidation kinetics and cycling stability of the material by countering the deactivation issue of $Mn_2O_3$. Furthermore, a Fe content of ~15 mol% added to $Mn_2O_3$ was identified as a minimum threshold for avoiding the formation of a low reactive $Mn_3O_4$ tetragonal spinel phase during reduction, which is detrimental to the reaction reversibility because of poor oxidation rate and yield. Noticeably, the $Mn_2O_3$ compounds with Fe content in the range 15-50 mol% could be cycled between bixbyite and cubic spinel phases without any reactivity losses during redox reactions. The addition of iron to Mn-based oxides also results in an increase of the reaction temperatures, while slightly lowering the gap in temperature between the reduction and oxidation step, which thereby reduces the sensible energy losses during the heating and cooling stages.

## IMDEA contribution

Current analysis addresses the following reversible redox chemical reaction:

$$6\ Mn_2O_3 \leftrightarrow 4\ Mn_3O_4 + O_2 \quad \Delta H=31.8\ kJ\ mol^{-1} \qquad (8)$$

Figure 13 shows typical thermogravimetric behaviour of $Mn_3O_4$ (Manganese Oxide $Mn_3O_4$-LH from Erachem Comilog SA was selected for this activity). Below 350 °C, there is a small weight decrease associated to the loss of some volatiles, free water and some of the combined water ($OH^-$ groups). Between 350 °C and 650 °C, the sample weight increases in two consecutive steps corresponding to the oxidation of the different Mn oxides co-existing in the sample until achieving the complete conversion to $Mn_2O_3$. Thermal reduction to $Mn_3O_4$ proceeds around 950 °C.

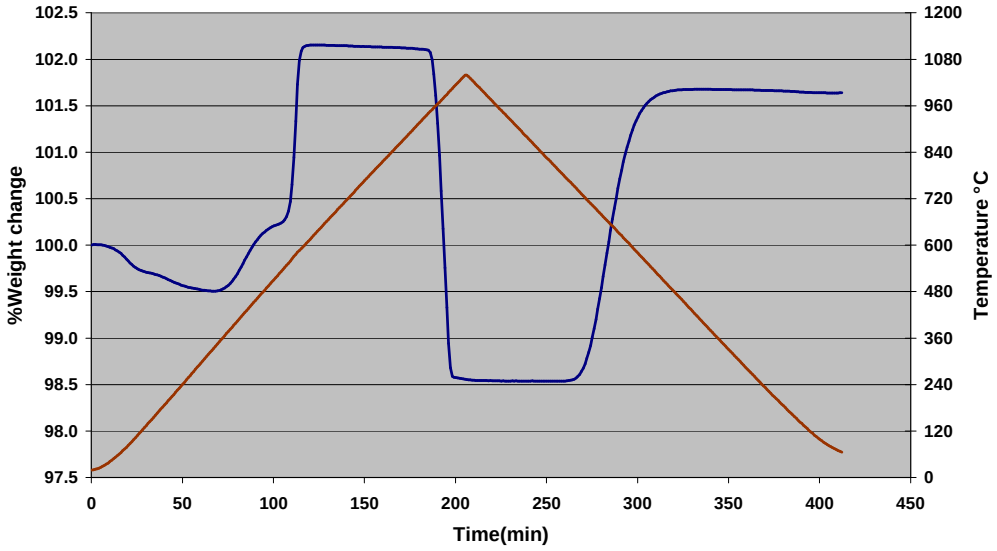


***Figure 13.*** *Typical TGA of a oxidation/reduction/oxidation cycle of $Mn_3O_4$ under air flow 75ml/min.*

*Chemical, physical and structural analysis*

Chemical analysis of $Mn_3O_4$-LH powders was obtained using a Perkin Elmer ICP-OES Spectrometer. It shows that the material contains 73.6% of Mn with an oxidation state of 2.7. Other minor chemical elements are presented in the material such as Ni, K, Na, Mg, Ca, Ba, Sr, Fe, Si, etc. Physical properties were measured by nitrogen adsorption-desorption isotherm with a Quantachrome QuadraSorb-S analyser. $Mn_3O_4$-LH powders present a total pore volume of 0.040 $cm^3/g$ and a specific surface area of 13.0 $m^2/g$. The structural analysis was performed by X-Ray Diffraction (XRD) (Figure 14) using a Bruker XRD diffractometer.

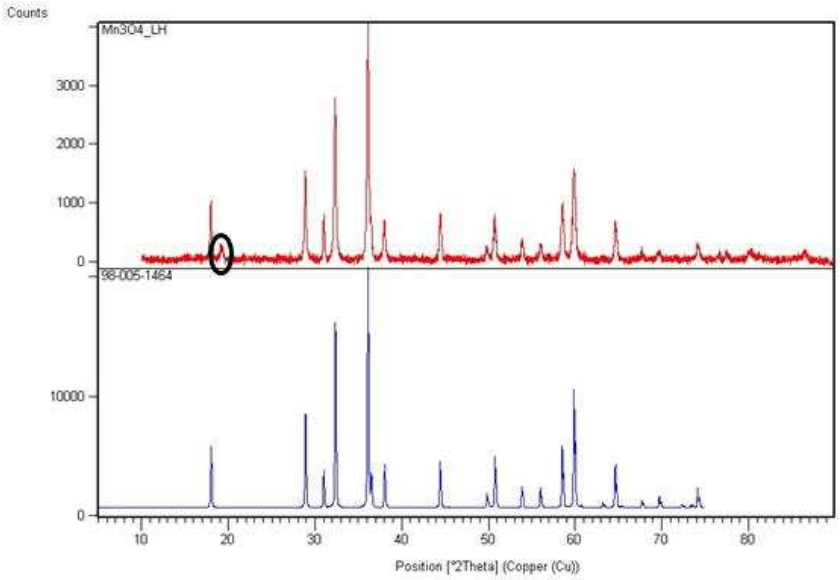


***Figure 14.*** *XRD difractogram of $Mn_3O_4$-LH.*

XRD peaks observed for $Mn_3O_4$-LH agree with diffraction patterns of $Mn_3O_4$ hausmannite (JCPDS- 98-005-1464), except a diffraction peak at 19.2º that is associated to impurities of $Mn_3O_4$-LH powders. According to 'Scherrer' estimation, $Mn_3O_4$-LH powders show a crystallite size around 40 nm, which well corresponds to the 'average' of primary crystals observed by scanning electron microscopy (SEM) and high-resolution scanning electron microscopy (HRSEM) (Figure 15).

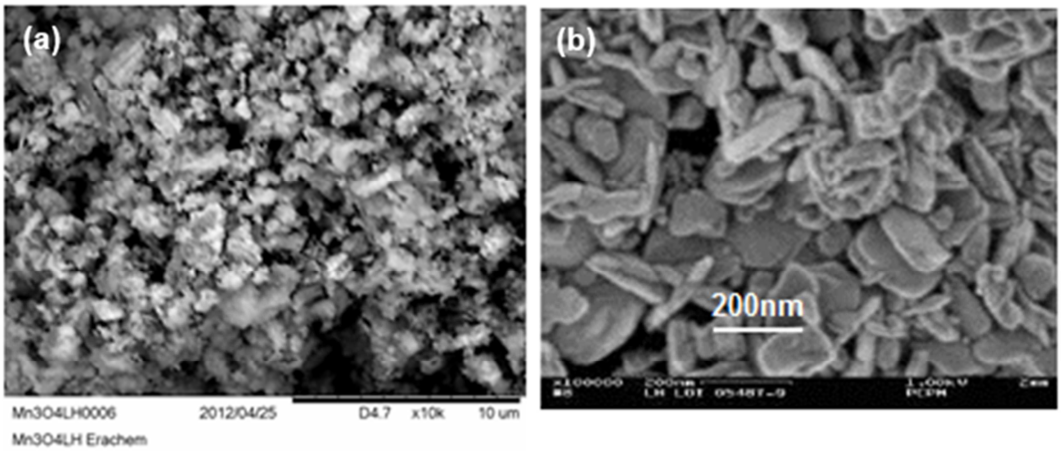


***Figure 15.*** *Micrographs of SEM (a) and HRSEM (b) of $Mn_3O_4$-LH.*

*Thermochemical behaviour of $Mn_3O_4$*

Thermogravimetric analyses (TGA) studies were performed using a SDT Q-600 from TA Instruments using a temperature program between 1000ºC to 550ºC with a rate of 10ºC/min in 100 ml/min air flow. Figure 16 (left) shows the thermogravimetric plot obtained for the 50 cycles of heating and cooling between 550 to 1000 ºC.

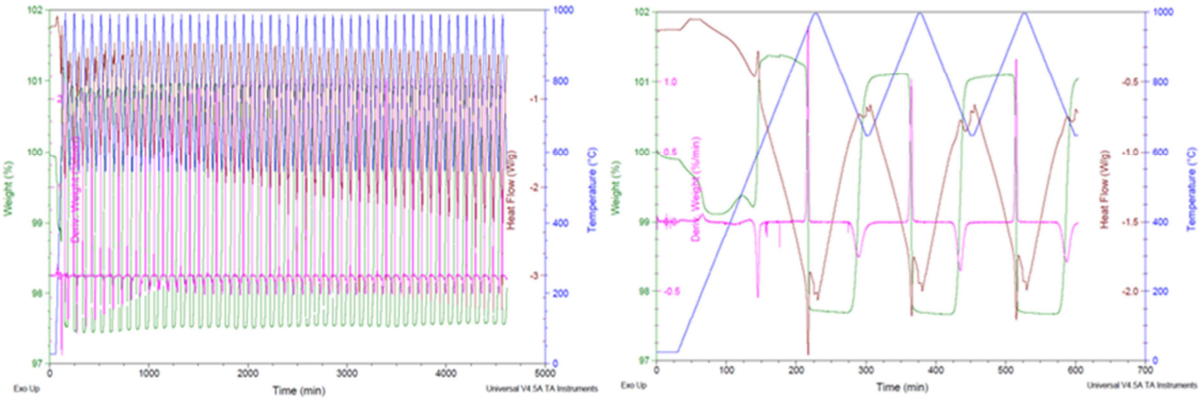


***Figure 16.*** *First cycles and 50 cycles of heating and cooling obtained for $Mn_3O_4$-LH.*

It can be observed that $Mn_3O_4$-LH maintains its good cyclability along the experiment. Figure 16 (right) shows a zoom on the first 3 heating/cooling cycles of $Mn_3O_4$-LH and the analyses shows an unusual behavior during the first cycle. This behavior is associated to impurities of $Mn_3O_4$-LH powders, agreeing with previous results of XRD.

$Mn_3O_4$-LH powders were subjected to a thermal treatment (Table 2) in order to eliminate the impurities in the powder.

**Table 2. Thermal treatments parameters applied to $Mn_3O_4$-LH.**

| Temperature | Period | Atmosphere |
|---|---|---|
| between 600 to 1000 ºC | between 30 minutes to 4 hours | Air or Argon |

The effect caused by the corresponding thermal treatment was measured by structural analysis and thermal characterization. Figure 17 shows the high temperature XRD results of $Mn_3O_4$-LH in air. Two different crystalline structure modifications were observed depending on the temperature. The first one takes place during the heating between 576 to 640° C, associated to the structure change from $Mn_3O_4$ (hausmannite) to $Mn_2O_3$ (bixbyite). The second change occurs during the cooling and it is associated to the re-change from $Mn_2O_3$ (bixbyite) to $Mn_3O_4$ (hausmannite).

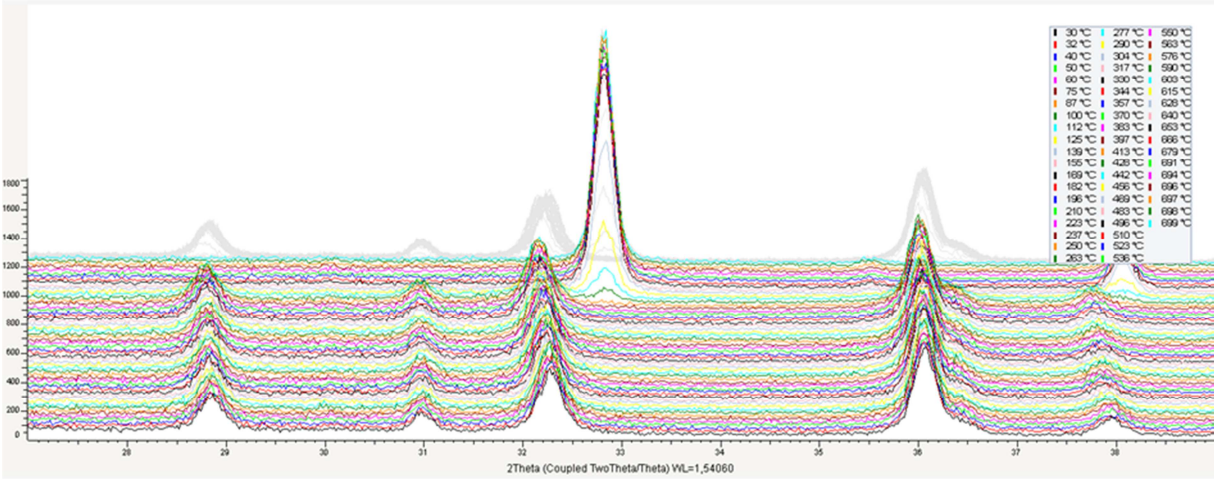


***Figure 17.*** *High Temperature XRD measurements of $Mn_3O_4$-LH in Argon.*

At higher temperatures, XRD analysis in argon, only shows a single crystalline phase up to 800 ºC associated to $Mn_3O_4$. This behavior is due to the absence of oxygen that prevents the oxidation of $Mn_3O_4$ to $Mn_2O_3$.

Crystal size of $Mn_3O_4$-LH with different thermal treatments was estimated using Scherrer estimation (Figure 18 (left)). The figure indicates that the thermal treatment produces an increment of the crystal size of $Mn_3O_4$-LH, which becomes more important when the temperature increases.

Thermogravimetric analyses of the thermally treated $Mn_3O_4$-LH points out that the thermochemical behaviour can be affected notably when the thermal treatment is performed at temperature higher that 600 ºC and residence times in the oven longer than 1 hour. Figure 18 (right) shows the TGA of $Mn_3O_4$-LH treated at 550 ºC during 30 minutes. After ten cycles, initial thermochemical properties $Mn_3O_4$-LH were maintained during the experiment compared to $Mn_3O_4$-LH without treatment.

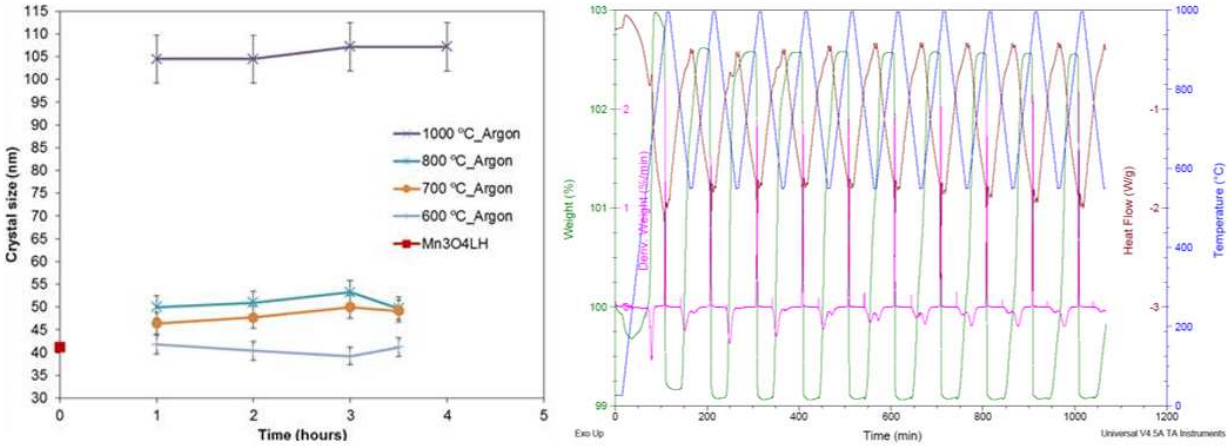


***Figure 18.*** *(Left) Crystal size of $Mn_3O_4$-LH powders with different thermal treatments in Argon; (right) Cyclability test of $Mn_3O_4$-LH treated at 600 ºC / 1 hour in Air.*

*The Manganese-ceria alternative*

A potential way to improve the material performance in terms of cyclability and/or working temperature of thermochemical materials is by mixing metal oxides of different melting points. This route could allow for stabilizing the overall particle structure avoiding sintering and enhancing the kinetics if one of the oxides acts as oxygen donor center. $Mn_3O_4$ and $CeO_2$ have been retained for analysing this concept.

The mixtures have been prepared by mechanical milling using a ball mixer PM 100 CM Retsch. Different parameters are under study such as Mn/Ce molar ratio, solvent molar ratio, milling time, spin rate (rpm) and thermal treatment.

First experimental results show the big effect of the manganese oxide content on the cyclability of the mixture $Mn_3O_4/CeO_2$; samples with a higher molar ratio of $Mn_3O_4$ showed better thermochemical performance. Thus, the molar relatio of mixture contents could be a key parameter to define the cyclability of the final material.

Further experimental activities are focussing on optimizing the synthesis and characterizing $Mn_3O_4/CeO_2$ mixtures depending on their chemical, physical and thermochemical properties.

## 3.3. Perovskites (CNRS)

$ABO_3$ structured perovskites present a high oxygen mobility and the ability to release and incorporate oxygen during cyclic endothermic reduction and exothermic oxidation. Further work on perovskites may lead to potential application to TES [23]. Sr and Ba-based perovskites were studied as oxygen sorbents [23-29]. $La_xSr_{1-x}Co_yMn_{1-y}O_{3-\delta}$ (LSCM) and $La_xSr_{1-x}Co_yFe_{1-y}O_{3-\delta}$ were presented by Babiniec et al (2015) [26] for their good reduction/oxidation reactivity. In our study, the objective was to assess the potential of Ba and/or Sr perovskites in solar thermochemical processes for energy storage application. The study aimed to identify the materials that exhibit the largest amounts of oxygen that can be released over the course of the reduction steps, and that at the same time can re-incorporate the same amount of oxygen in a completely reversible way. The reversibility of reduction and oxidation reactions was investigated to screen the most attractive materials. The studied perovskite based materials with different compositions considered were $SrMnO_{3-\delta}$, $SrCoO_{3-\delta}$, $SrFeO_{3-\delta}$, $BaCoO_{3-\delta}$, $BaFeO_{3-\delta}$, $BaMnO_{3-\delta}$, $SrCo_{0.8}Fe_{0.2}O_{3-\delta}$, $SrCo_{0.2}Fe_{0.8}O_{3-\delta}$, $Ba_{0.5}Sr_{0.5}CoO_{3-\delta}$, $Ba_{0.5}Sr_{0.5}FeO_{3-\delta}$, $Ba_{0.5}Sr_{0.5}Co_{0.8}Fe_{0.2}O_{3-\delta}$ and $Ba_{0.5}Sr_{0.5}Co_{0.2}Fe_{0.8}O_{3-\delta}$ [30].

The $O_2$ exchange of Co-based perovskites is rapid, and it seems that there is a transition in the oxidation state when reaching a given temperature. In contrast, the $O_2$ exchange rate of Fe-based perovskites is corresponding to the temperature variation, which points out the fast kinetics as the equilibrium state is reached for each temperature of the non-isothermal profile. Finally, the Mn-based systems are almost unchanged during the course of the redox cycles in the considered temperature range, which denotes their high stability and unsuitability for thermochemical redox cycling under the given reaction conditions (Table 3).

**Table 3. $O_2$ exchange capacity and difference in non-stoichiometry of different perovskites samples (mol O / mol perovskites)**

| Samples | 1st cycle | | | 2nd cycle | |
|---|---|---|---|---|---|
| | Red. | 1st step oxid. (600°C) | 2nd step oxid. | Red. | Oxid. |
| $SrMnO_{3-\delta}$ | 0.06 | 0.03 | 0 | - | - |
| $SrCoO_{3-\delta}$ | 0.33 | 0.21 | 0.03 | 0.18 | 0.17 |
| $SrFeO_{3-\delta}$ | 0.24 | 0.16 | 0.08 | 0.19 | 0.18 |
| $BaMnO_{3-\delta}$ | 0.11 | 0 | 0 | - | - |
| $BaCoO_{3-\delta}$ | 0.47 | 0.49 | 0.02 | 0.49 | 0.37 |
| $BaFeO_{3-\delta}$ | 0.45 | 0.02 | 0.12 | 0.14 | 0.12 |
| SCF-82 | 0.37 | 0.14 | 0.1 | 0.19 | 0.19 |
| SCF-28 | 0.36 | 0.17 | 0.1 | 0.23 | 0.21 |
| BSC-55 | 0.45 | 0.26 | 0.03 | 0.29 | 0.22 |
| BSF-55 | 0.27 | 0.12 | 0.12 | 0.24 | 0.24 |
| BSCF-5582 | 0.23 | 0.11 | 0.1 | 0.18 | 0.2 |
| BSCF-5528 | 0.26 | 0.15 | 0.09 | 0.19 | 0.2 |

The XRD patterns of perovskites with different compositions are shown in Fig.19. The main peaks observed in all diffractograms can be attributed to the characteristic perovskite structure. The main reflection difference can also be observed, which may be originated from the distortions of the ideal cubic perovskites. $SrFeO_{3-\delta}$ shows the strongest intensity, while the $BaFeO_{3-\delta}$ is the weakest among all the samples. The weak peak at about $2\theta=18.3^{o}$ is reflection of (100) surface, and the peaks at $2\theta=32.8^{o}$, $40.5^{o}$, $47.1^{o}$, $53.1^{o}$, $58.6^{o}$, $68.8^{o}$, $78.3^{o}$, $83.7^{o}$, and $96.8^{o}$ reflect (110), (111), (200), (210), (211), (220), (310), (311) and (321) crystal surface of $SrFeO_{2.97}$ with cubic structure respectively. On the pattern of $SrCoO_{3-\delta}$, the peak appearing at $2\theta=28.5^{o}$ is reflection of (101) surface; the peak at $2\theta=43.8^{o}$ is reflection of (201) surface, and the peak at $55.6^{o}$ is from (112) of $SrCoO_{2.52}$ with hexagonal crystal structure. The peaks of $SrMnO_3$ and $BaMnO_3$ are somewhat complicated, but they still can be identified as $SrMnO_3$ and $BaMnO_3$ with hexagonal structure. The other samples are analyzed with the same procedure. Main crystal structure of these materials has been determined from the PXRD diagram databases of ICDD, as listed in Table 4.

**Table 4. Main crystal phase of different perovskites samples by ICDD**

| Samples | Abbreviation | Reference code | Main crystal phase by XRD |
|---|---|---|---|
| $SrMnO_{3-\delta}$ | | 00-024-1213 | $SrMnO_3$ |
| $SrCoO_{3-\delta}$ | | 00-040-1018 | $SrCoO_{2.52}$ |
| $SrFeO_{3-\delta}$ | | 00-040-0905 | $SrFeO_{2.97}$ |
| $BaCoO_{3-\delta}$ | | 01-074-9199 | $Ba_5Co_5O_{14}$ |
| $BaFeO_{3-\delta}$ | | 00-020-0131 | $BaFeO_{2.64}$ |
| $BaMnO_{3-\delta}$ | | 00-014-0228 | $BaMnO_3$ |
| $SrCo_{0.8}Fe_{0.2}O_{3-\delta}$ | SCF-82 | 00-040-1018 | $SrCoO_{2.52}$ |
| $SrCo_{0.2}Fe_{0.8}O_{3-\delta}$ | SCF-28 | 00-040-0905 | $SrFeO_{2.97}$ |
| $Ba_{0.5}Sr_{0.5}CoO_{3-\delta}$ | BSC-55 | 00-040-1018 | $SrCoO_{2.52}$ |
| $Ba_{0.5}Sr_{0.5}FeO_{3-\delta}$ | BSF-55 | 00-020-0127 | $BaFeO_{2.88}$ |
| $Ba_{0.5}Sr_{0.5}Co_{0.8}Fe_{0.2}O_{3-\delta}$ | BSCF-5582 | 00-055-0563 | $Ba_{0.5}Sr_{0.5}Co_{0.8}Fe_{0.2}O_{2.55}$ |
| $Ba_{0.5}Sr_{0.5}Co_{0.2}Fe_{0.8}O_{3-\delta}$ | BSCF-5528 | 00-055-0563 | $Ba_{0.5}Sr_{0.5}Co_{0.8}Fe_{0.2}O_{2.55}$ |

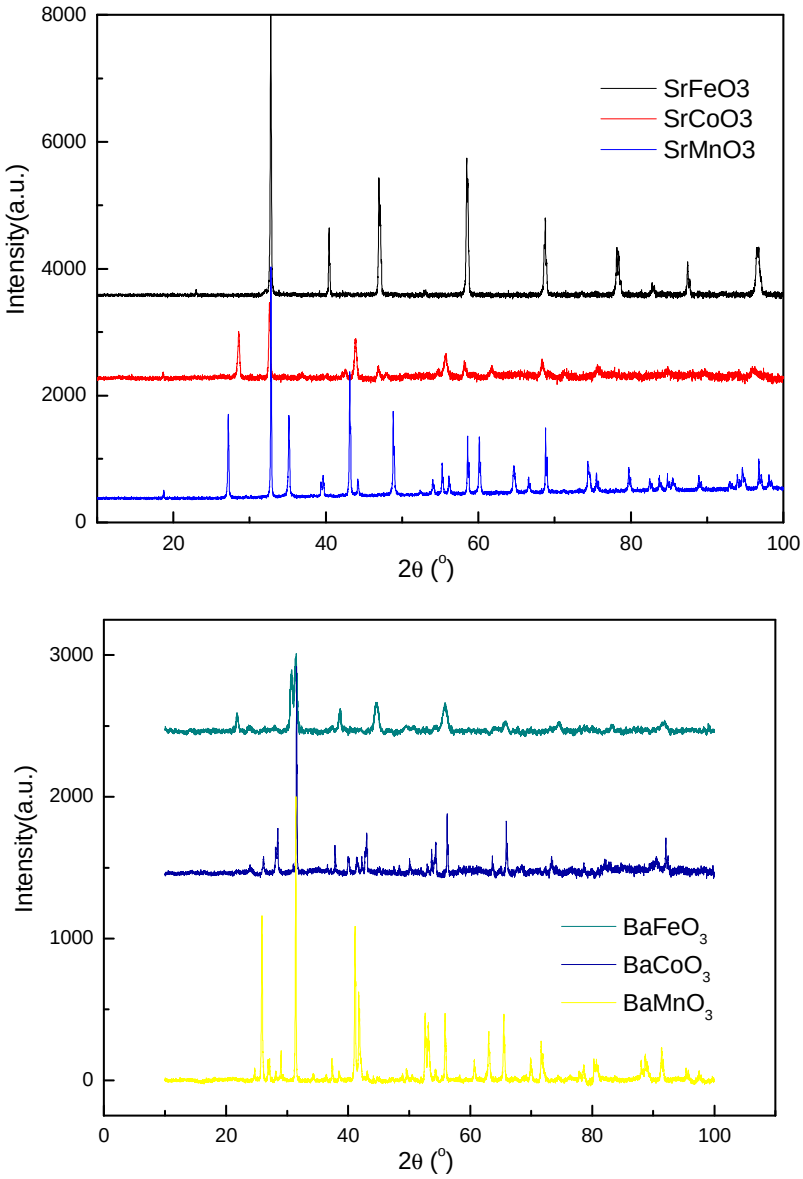


***Figure 19.*** *XRD patterns of non-substituted perovskites samples.*

Fig. 20 shows the different redox behavior ($O_2$ release and absorption) of $SrBO_{3-\delta}$ (B = Fe, Co, and Mn) perovskites that were measured using TGA. In the first redox cycle (0-125min under Ar, reduction to 950°C), $SrCoO_{3-\delta}$ releases 2.79 mass% of $O_2$, which is the largest amount among the three samples. $SrFeO_{3-\delta}$ and $SrMnO_{3-\delta}$ release 1.79 and 0.38 mass% of $O_2$, under the same conditions. The following oxidation behaviors of the three samples at 600°C are also clearly different. For $SrCoO_{3-\delta}$, it can be oxidized greatly (1.72 mass%) in a short time when the atmosphere is switched from Ar to 20%$O_2$ at 600 $^oC$. Little part (0.31 mass%) can be further oxidized when the temperature decreases from 600$^oC$ to 300$^oC$. For $SrFeO_{3-\delta}$, besides the part of oxidation (1.33 mass%) when the atmosphere is switched from Ar to 20%$O_2$ at 600$^oC$, it can be further oxidized (0.69 mass%) with a certain rate when the temperature decreases from 600$^oC$ to 300$^oC$. As for $SrMnO_{3-\delta}$, it shows very poor oxidation behavior through the course of the experiment. Only about 0.11 mass% $O_2$ is recovered. For the second redox cycle (125-225 min under 20% $O_2$ throughout), their behaviors are also

different from each other. $SrCoO_{3-\delta}$ releases $O_2$ constantly while the temperature increases from 300°C to 1050°C with a sharp mass loss when the temperature approaches 1050°C. The total mass loss is about 1.82% and then it is nearly fully recovered when the temperature decreases to 300°C. $SrFeO_{3-\delta}$ keeps a stable reaction rate during the temperature increase and decrease periods. The reaction is perfectly reversible and 1.45 mass% $O_2$ is released and adsorbed during the course of heat treatment. In contrast, $SrMnO_{3-\delta}$ shows a poor $O_2$ release ability again and the mass loss cannot be even recovered when the temperature decreases. The results show that $SrFeO_{3-\delta}$ and $SrCoO_{3-\delta}$ can be good candidates for oxygen exchange during solar thermochemical conversion while $SrMnO_{3-\delta}$ is not suitable.

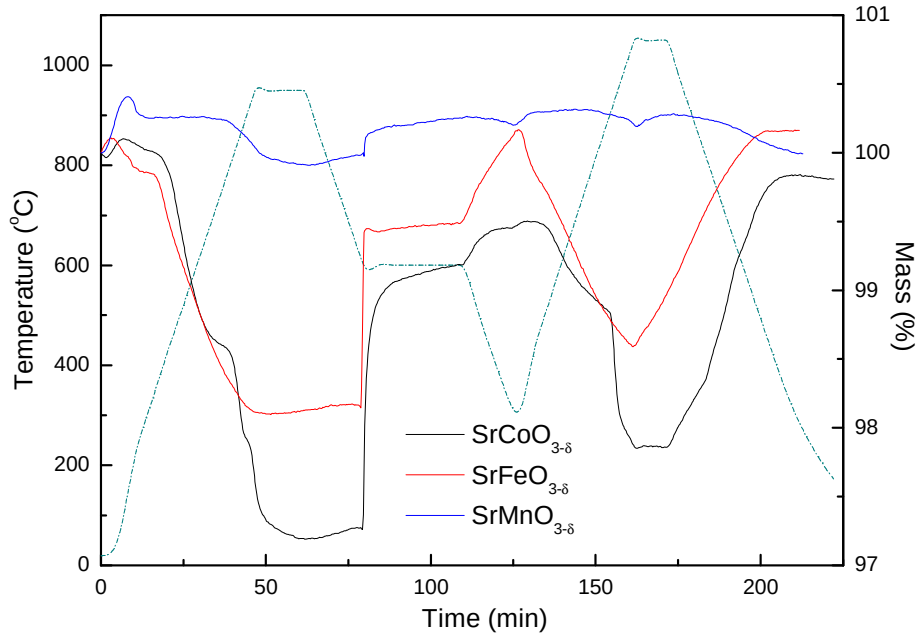


***Figure 20.*** *Redox behavior of $SrBO_{3-\delta}$ (B=Fe, Co and Mn) perovskites.*

Perovskites of the $BaBO_3$ series are then discussed. Fig. 21 shows the different $O_2$ release and absorption of $BaBO_{3-\delta}$ perovskites that were measured using TGA. The $BaCoO_{3-\delta}$ shows the largest redox ability among the three samples again. During the first redox cycle, the mass variation reaches 3.13% and it has been recovered entirely during oxidation at 600°C; reasonably, a little fraction (0.13 mass%) is further oxidized when the temperature decreases to 300°C. $BaFeO_{3-\delta}$ has larger $O_2$ release capability than $SrFeO_{3-\delta}$ in the first redox cycle; while it shows very poor re-oxidation ability at 600°C, and the oxidation occurs mainly upon cooling below 600°C. The $BaMnO_{3-\delta}$ shows very poor redox ability, which is even worse than $SrMnO_{3-\delta}$. It seems that it cannot be reduced or oxidized during the course of the temperature-programmed experiment. The results thus indicate that Co-based perovskites are the best candidates for oxygen exchange applied to solar thermochemical energy conversion and storage, which is consistent with the prediction of Ezbiri *et al.* [31].

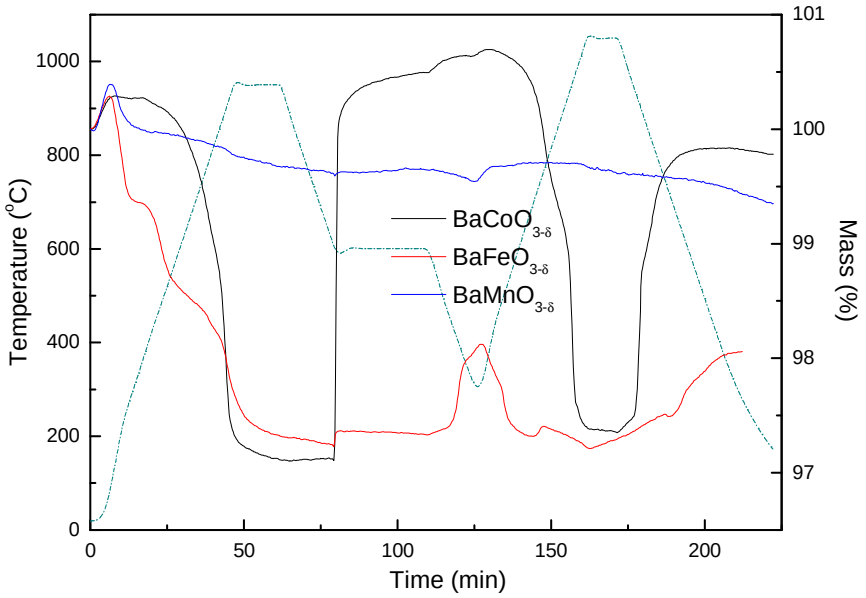


***Figure 21.*** *Redox behavior of $BaBO_{3-\delta}$ (B=Fe, Co and Mn) perovskites.*

Due to the high tolerance ability of $ABO_3$ structure, a common method consists in improving the different properties of perovskites-based materials by part substitution of A or B sites with other elements and changing the $ABO_3$ formula into AA'$BO_3$ or ABB'$O_3$. As $BaFeO_{3-\delta}$, $BaCoO_{3-\delta}$, $SrFeO_{3-\delta}$ and $SrCoO_{3-\delta}$ show better redox ability among the tested perovskites materials, they are chosen as the reference systems for substitution. Half of the Ba in the $BaFeO_{3-\delta}$ and $BaCoO_{3-\delta}$ was substituted by Sr in the A-site, $Ba_{0.5}Sr_{0.5}FeO_{3-\delta}$ and $Ba_{0.5}Sr_{0.5}CoO_{3-\delta}$ samples were thereby obtained. Similarly, part substitution in the B-site brings the $SrCo_{0.8}Fe_{0.2}O_{3-\delta}$ and $SrCo_{0.2}Fe_{0.8}O_{3-\delta}$. Their XRD patterns are presented in Fig. 22. According to ICDD database, their detailed formula (oxygen stoichiometry) are also determined and listed in Table 4.

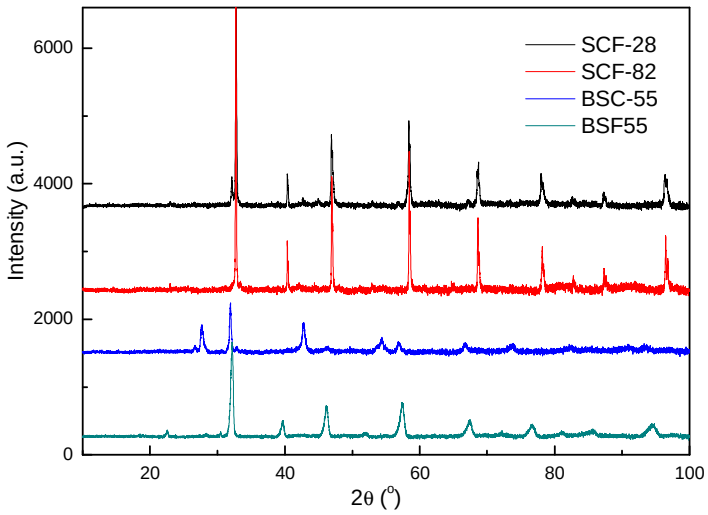


***Figure 22.*** *XRD patterns of A site or B site substituted perovskites.*

Fig. 23 displays the TGA results of A or B site substituted samples. In Fig.23A, the substitution of Sr does not change the redox process of $Ba_{0.5}Sr_{0.5}CoO_{3-\delta}$ and $Ba_{0.5}Sr_{0.5}FeO_{3-\delta}$ but influences the redox reaction extent as expected. $Ba_{0.5}Sr_{0.5}CoO_{3-\delta}$ releases 3.49 mass% $O_2$ in the first redox cycle, which is higher than for $BaCoO_{3-\delta}$ and $SrCoO_{3-\delta}$. The $O_2$ recovery then amounts to 2.47 mass% at 600 $^oC$, which is larger than that of $SrCoO_{3-\delta}$ but smaller than that of $BaCoO_{3-\delta}$. In the second cycle, it releases 2.09 mass% $O_2$ and recovers 1.90 mass% $O_2$. The performance is between $BaCoO_{3-\delta}$ and $SrCoO_{3-\delta}$. For $Ba_{0.5}Sr_{0.5}FeO_{3-\delta}$, it releases 2.05 mass% $O_2$ in the first redox cycle, which is close to $SrFeO_{3-\delta}$ but smaller than $BaFeO_{3-\delta}$. While 1.90 mass% $O_2$ is recovered down to 300$^oC$, which is close to that of $SrFeO_{3-\delta}$ but much higher than that of $BaFeO_{3-\delta}$. Further, in the second cycle, it releases 1.77 mass% $O_2$ and gets back 1.86 mass% $O_2$. The performance is better than $BaFeO_{3-\delta}$ and $SrFeO_{3-\delta}$. In general, the coexistence of Ba and Sr has positive effect on the redox performance of $Ba_{0.5}Sr_{0.5}CoO_{3-\delta}$ and $Ba_{0.5}Sr_{0.5}FeO_{3-\delta}$.

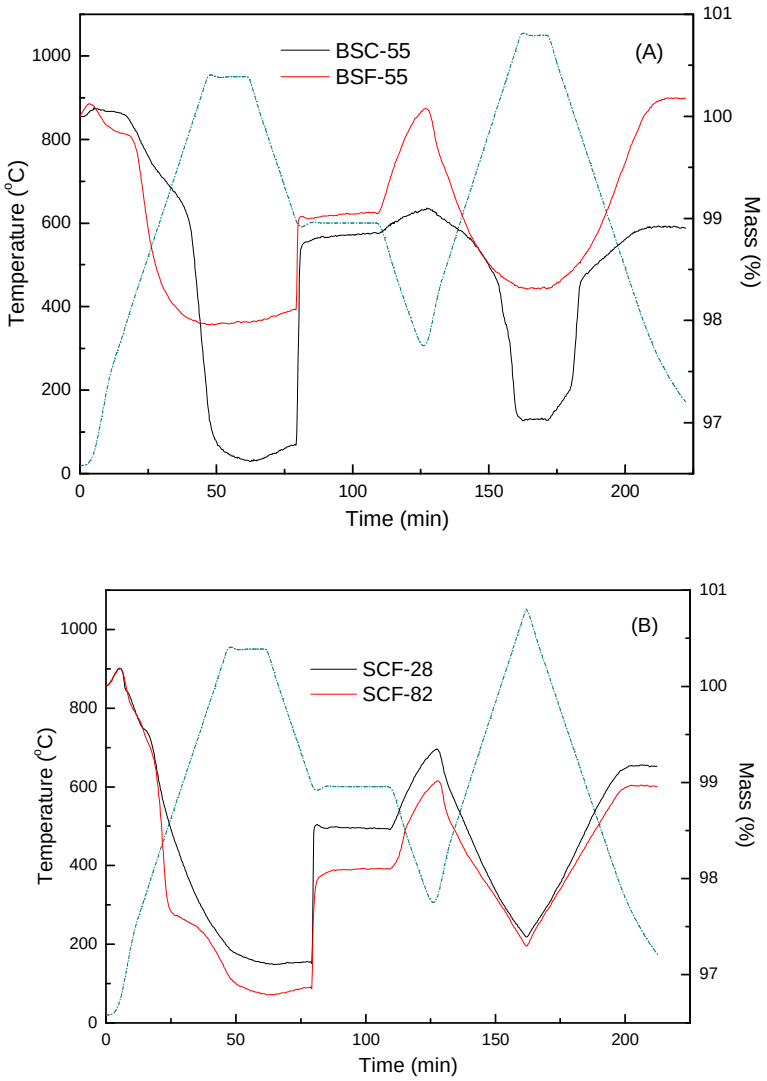


***Figure 23.*** *Redox behavior of A-site or B-site substituted perovskites (A) $Ba_{0.5}Sr_{0.5}FeO_{3-\delta}$ and $Ba_{0.5}Sr_{0.5}CoO_{3-\delta}$ (A-site substituted); (B) $SrCo_{0.8}Fe_{0.2}O_{3-\delta}$ and $SrCo_{0.2}Fe_{0.8}O_{3-\delta}$ (B-site substituted).*

Next, partial substitution of cobalt in $SrCoO_{3-\delta}$ by iron leads to a change in the redox process of $SrCo_{0.8}Fe_{0.2}O_{3-\delta}$ and $SrCo_{0.2}Fe_{0.8}O_{3-\delta}$, which follows the pattern of $SrFeO_{3-\delta}$ (Fig. 23B). In the first redox cycle, it is first partially oxidized at 600°C with an equilibrium reached rapidly, and then further oxidized with a constant rate when the temperature decreases from 600°C to 300°C. Similarly in the second cycle, both the oxidation and reduction processes are realized with constant rates following the temperature profile, which highlights the rapid equilibrium reached for each temperature.

Then, we partially substituted the A and B sites of $ABO_3$ perovskites at the same time, and obtained $Ba_{0.5}Sr_{0.5}Co_{0.8}Fe_{0.2}O_{3-\delta}$ and $Ba_{0.5}Sr_{0.5}Co_{0.2}Fe_{0.8}O_{3-\delta}$, which are well known anode materials for the applications in fuel cells. The XRD patterns are presented in Fig. 24, which is consistent to the previous studies. The TGA results are presented in Fig. 25. The redox behavior of the two samples follows the characteristics of $SrCoO_{3-\delta}$ and $SrFeO_{3-\delta}$. In the first redox cycle, the oxidation process follows the characteristic of $SrFeO_{3-\delta}$. While in the second redox cycle, the process shows a combined effect of $SrCoO_{3-\delta}$ and $SrFeO_{3-\delta}$. It releases $O_2$ with a quasi-constant rate during the temperature increase, and finally absorbs $O_2$ with a quasi-constant rate during the temperature decrease. The phenomenon is more pronounced on the profile of $Ba_{0.5}Sr_{0.5}Co_{0.8}Fe_{0.2}O_{3-\delta}$, which contains more cobalt. Unfortunately, this phenomenon does not help for the redox ability of $Ba_{0.5}Sr_{0.5}Co_{0.8}Fe_{0.2}O_{3-\delta}$ and $Ba_{0.5}Sr_{0.5}Co_{0.2}Fe_{0.8}O_{3-\delta}$. In fact, the redox ability of the two samples has been restrained greatly. $Ba_{0.5}Sr_{0.5}Co_{0.2}Fe_{0.8}O_{3-\delta}$ only releases 1.81 mass% $O_2$ and recovers 1.57% in the first redox cycle; $Ba_{0.5}Sr_{0.5}Co_{0.8}Fe_{0.2}O_{3-\delta}$ releases 1.95 mass% $O_2$ and recovers 1.80% in the first redox cycle. All the values are much lower than those of samples without substitution under the same conditions. The results may indicate that substitution of A and B sites of perovskite-based materials does not always favor the redox ability.

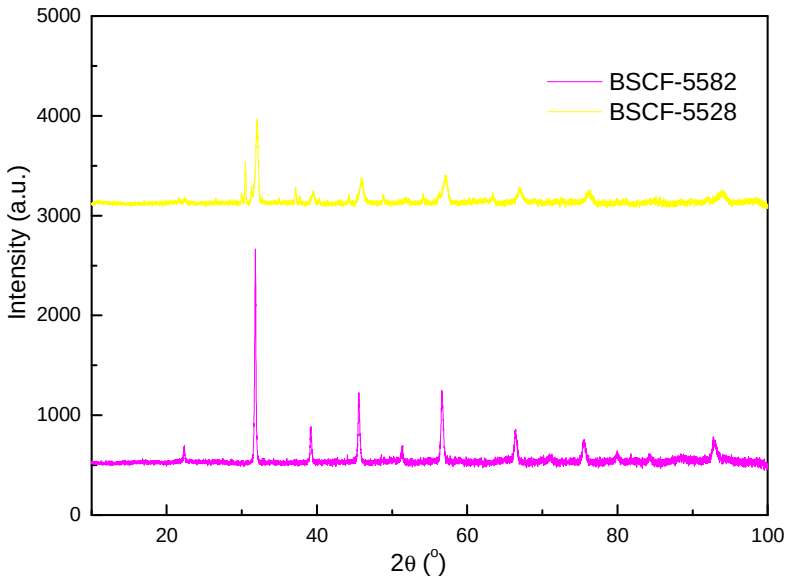


***Figure 24.*** *XRD patterns of $Ba_{0.5}Sr_{0.5}Co_{0.8}Fe_{0.2}O_{3-\delta}$ and $Ba_{0.5}Sr_{0.5}Co_{0.2}Fe_{0.8}O_{3-\delta}$.*

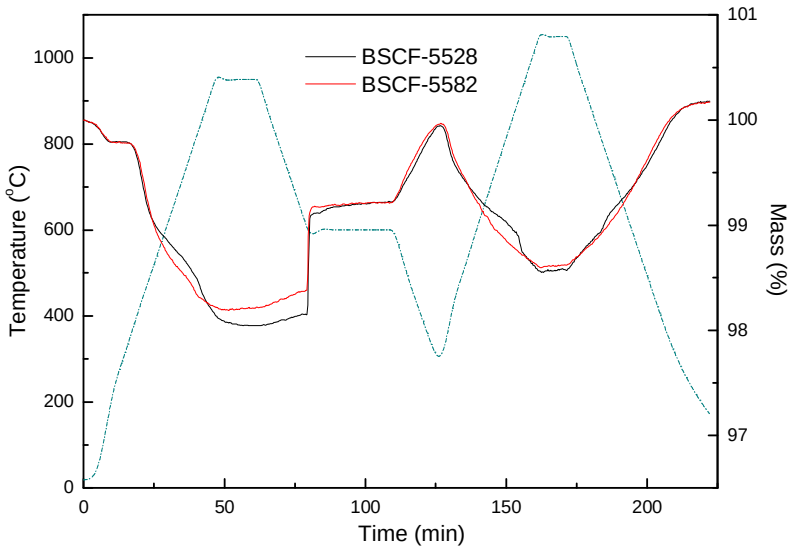


***Figure 25.*** *Redox behavior of $Ba_{0.5}Sr_{0.5}Co_{0.8}Fe_{0.2}O_{3-\delta}$ and $Ba_{0.5}Sr_{0.5}Co_{0.2}Fe_{0.8}O_{3-\delta}$ perovskites.*

In general, Co-based and Fe-based perovskites show high redox ability here, while their redox patterns are clearly different from each other. The $O_2$ release and absorption of Co-based perovskites is rapid and seems like that there is a "switch" when reaching a given temperature; while the oxygen stoichiometry of Fe-based perovskites is gradually changed according to the equilibrium following the temperature profile. To understand the redox behavior of these different perovskites materials, the mole values of oxygen atom lost per mol perovskites during different steps are calculated. The results are listed in Table 3 (page 27). It can be seen that the three Co-based samples ($SrCoO_{3-\delta}$, $BaCoO_{3-\delta}$ and $Ba_{0.5}Sr_{0.5}CoO_{3-\delta}$) have adsorbed 0.21 mol, 0.47 mol and 0.26 mol monatomic oxygen per mol samples at 600°C. While only 0.03 mol, 0.02 mol and 0.03 mol monatomic oxygen are further adsorbed when the temperature decreases from 600°C to 300°C. It means that most part of oxidation is finished at a certain temperature (600°C). As for the three Fe-based samples ($SrFeO_{3-\delta}$, $BaFeO_{3-\delta}$ and $Ba_{0.5}Sr_{0.5}FeO_{3-\delta}$), the monatomic oxygen adsorption mole amount during the two oxidation steps in the first redox cycle are 0.16:0.08, 0.02:0.12 and 0.12:0.12, respectively. The second step (600°C to 300°C) clearly plays a more important role. Further, among Fe and Co, it is the Fe that determines the redox pattern. All the perovskites follow the pattern of $SrFeO_{3-\delta}$ as long as Fe exists in the sample.

Besides, substitution effects of A or B sites on the redox behavior can also be seen from the table 3. Partial substitution of $SrCoO_{3-\delta}$ by Fe only slightly improves the redox behavior of $SrCo_{0.8}Fe_{0.2}O_{3-\delta}$. In contrast, partial substitution of $SrFeO_{3-\delta}$ by Co has significant effect on the $SrCo_{0.2}Fe_{0.8}O_{3-\delta}$. The coexistence of Fe and Co is beneficial for the redox behavior of Co-based and Fe-based perovskites. For A site substituted $Ba_{0.5}Sr_{0.5}CoO_{3-\delta}$ and $Ba_{0.5}Sr_{0.5}FeO_{3-\delta}$, it depends on the point of view. If we treat them as $SrBO_3$ substituted by Ba, we get better results than with non-substituted samples. If we treat them as $BaBO_3$ substituted by Sr, we get worse results. In general, it can be concluded that existence of Ba is beneficial for the redox behavior.

According to the main crystal phase determined by XRD databases of ICDD and the monatomic oxygen release per mol of samples in Table 3, the redox reaction equation can be written as follows (taking $SrCoO_{3-\delta}$ as example):

$$SrCoO_{2.52} \rightarrow SrCoO_{2.19} + \frac{0.33}{2}O_2 \quad \text{Reduction} \tag{9}$$

$$SrCoO_{2.19} + 0.17O_2 \rightarrow SrCoO_{2.43} \quad \text{Oxidation} \tag{10}$$

The redox equations of the other samples have also been written with the same procedure and are listed in Table 5. For convenience, only the variation of oxygen stoichiometry of the different samples is indicated.

**Table 5. Crystal phase variation of different samples during redox cycle**

| Sample | Variation of crystal phase during 1st redox cycle | No. |
|---|---|---|
| $SrCoO_{3-\delta}$ | $SrCoO_{2.52} \rightarrow SrCoO_{2.19} \rightarrow SrCoO_{2.43}$ | (1) |
| $SrFeO_{3-\delta}$ | $SrFeO_{2.97} \rightarrow SrFeO_{2.73} \rightarrow SrFeO_{2.97}$ | (2) |
| $BaCoO_{3-\delta}$ | $BaCoO_{2.8} \rightarrow BaCoO_{2.33} \rightarrow BaCoO_{2.82}$ | (3) |
| $BaFeO_{3-\delta}$ | $BaFeO_{2.64} \rightarrow BaFeO_{2.19} \rightarrow BaFeO_{2.33}$ | (4) |
| SCF-82 | $SrCoO_{2.52} \rightarrow SrCoO_{2.15} \rightarrow SrCoO_{2.39}$ | (5) |
| SCF-28 | $SrFeO_{2.97} \rightarrow SrFeO_{2.61} \rightarrow SrFeO_{2.88}$ | (6) |
| BSC-55 | $SrCoO_{2.52} \rightarrow SrCoO_{2.07} \rightarrow SrCoO_{2.36}$ | (7) |
| BSF-55 | $BaFeO_{2.88} \rightarrow BaFeO_{2.61} \rightarrow BaFeO_{2.87}$ | (8) |
| BSCF-5582 | $Ba_{0.5}Sr_{0.5}Co_{0.8}Fe_{0.2}O_{2.55} \rightarrow Ba_{0.5}Sr_{0.5}Co_{0.8}Fe_{0.2}O_{2.32} \rightarrow Ba_{0.5}Sr_{0.5}Co_{0.8}Fe_{0.2}O_{2.53}$ | (9) |
| BSCF-5528 | $Ba_{0.5}Sr_{0.5}Co_{0.8}Fe_{0.2}O_{2.55} \rightarrow Ba_{0.5}Sr_{0.5}Co_{0.8}Fe_{0.2}O_{2.29} \rightarrow Ba_{0.5}Sr_{0.5}Co_{0.8}Fe_{0.2}O_{2.53}$ | (10) |

Note: variation for $SrMnO_3$ and $BaMnO_3$ are not listed due to their poor redox ability.

The changes of oxygen stoichiometry may reflect the distortion tolerance of the perovskites crystal structure. Among all the samples, the crystal structure of $SrFeO_{3-\delta}$, $SrCo_{0.2}Fe_{0.8}O_{3-\delta}$, $BaCoO_{3-\delta}$, $Ba_{0.5}Sr_{0.5}FeO_{3-\delta}$, $Ba_{0.5}Sr_{0.5}Co_{0.8}Fe_{0.2}O_{3-\delta}$ and $Ba_{0.5}Sr_{0.5}Co_{0.2}Fe_{0.8}O_{3-\delta}$ can be fully restored during re-oxidation; while the other four samples ($SrCoO_{3-\delta}$, $BaFeO_{3-\delta}$, $SrCo_{0.8}Fe_{0.2}O_{3-\delta}$ and $Ba_{0.5}Sr_{0.5}CoO_{3-\delta}$) cannot, as the reaction seems to be not reversible. For the fully restored samples, the minimum oxygen number of the main crystal phase during reduction is 2.29 ($Ba_{0.5}Sr_{0.5}Co_{0.2}Fe_{0.8}O_{3-\delta}$); while the maximum oxygen number of the main crystal phase after reduction in the latter four samples is 2.19 ($SrCoO_{3-\delta}$ and $BaFeO_{3-\delta}$). The range of 2.19-2.29 seems to be the threshold for these samples. Below oxygen number 2.19, the perovskites crystal structure may have been altered and it cannot be fully recovered under these conditions. In fact, this phenomenon was previously pointed out in previous studies, as the formula of $ABO_{2+\varepsilon}$ was rather used to indicate this variation [32]. Compared to Fe-based systems, it seems that the crystal structure of Co-based systems such as $SrCoO_{3-\delta}$, $SrCo_{0.8}Fe_{0.2}O_{3-\delta}$ and $Ba_{0.5}Sr_{0.5}CoO_{3-\delta}$ is easier to be altered. Further, within its distortion tolerance range, the phase change of perovskites is inclined to jump from one stable crystal structure to another, which determines the oxygen release/adsorption content. The main non-stoichiometry formulas observed during redox process are $SrCoO_{2.8}$, $SrCoO_{2.52\pm0.03}$, $SrCoO_{2.33\pm0.03}$ (Co-based systems), and $SrFeO_{2.97}$, $SrFeO_{2.88}$, $SrFeO_{2.64\pm0.03}$ (Fe-based systems), respectively.

The variation of the main crystal phase can be partially disclosed by the room temperature XRD analysis of samples after thermal cycles. The variation of the intensity and the position of characteristic peaks can be used to highlight the modification of the crystal structure. The XRD patterns of the different samples after TG have been recorded under room temperature, as shown in Fig. 26. Compared to the patterns of fresh samples in Fig. 19, Fig. 22 and Fig. 24, the position and intensity of characteristic peaks of $SrFeO_{3-\delta}$, $SrCo_{0.2}Fe_{0.8}O_{3-\delta}$, $SrCo_{0.8}Fe_{0.2}O_{3-\delta}$, $Ba_{0.5}Sr_{0.5}FeO_{3-\delta}$ and $Ba_{0.5}Sr_{0.5}Co_{0.8}Fe_{0.2}O_{3-\delta}$ do not change significantly, which indicates that their crystal structures have not been altered during reversible reaction. In contrast, the intensity and position of characteristic peaks of $BaCoO_{3-\delta}$, $BaFeO_{3-\delta}$, $Ba_{0.5}Sr_{0.5}CoO_{3-\delta}$ and $Ba_{0.5}Sr_{0.5}Co_{0.2}Fe_{0.8}O_{3-\delta}$ are clearly influenced. Their crystal structure should thus have been greatly modified.

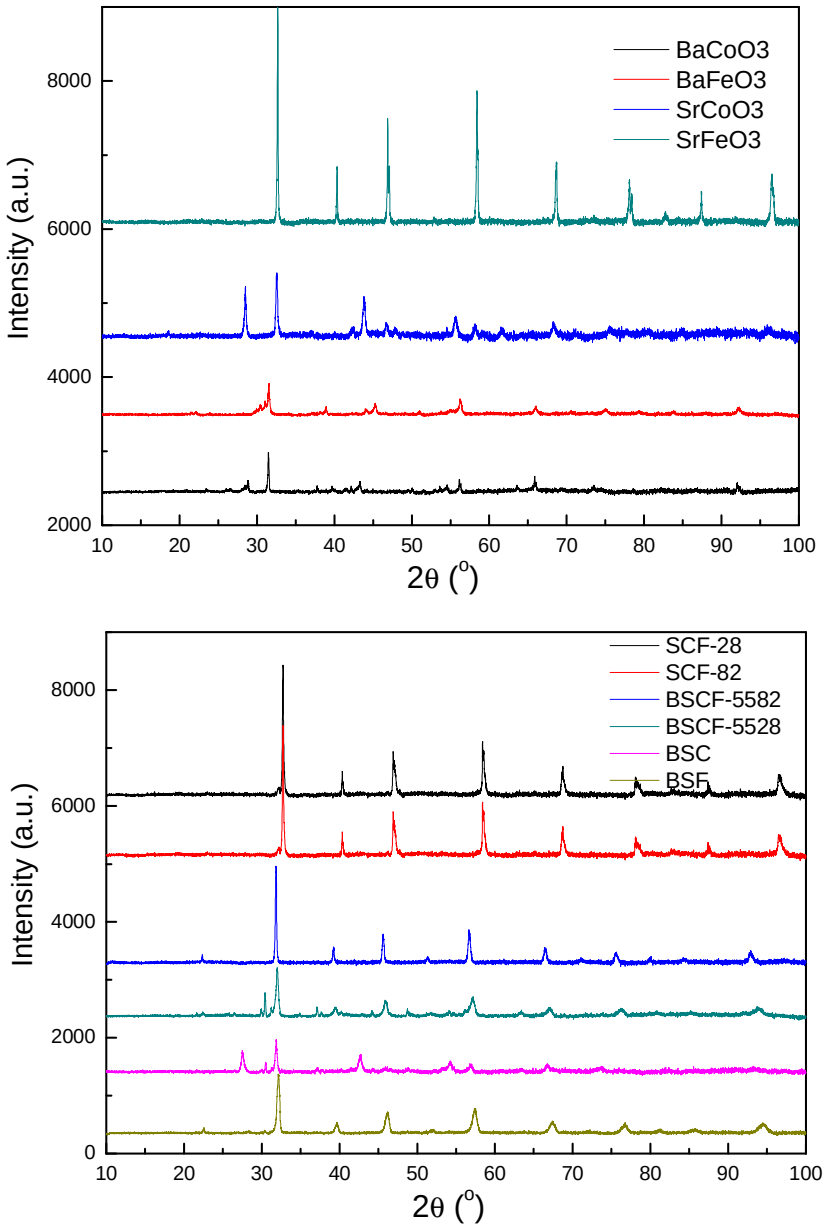


***Figure 26.*** *XRD patterns of different samples after thermal cycling TG analysis.*

## 4. Integration of thermochemical storage systems: a case study[1] (PSI)

This case study investigates how the gas-solid contacting pattern in a thermochemical storage (TCS) system influences (1) the integration of the storage into a concentrated solar power (CSP) plant and (2) the resulting performance of the CSP plant. The manganese oxide redox-cycle

$$6\ Mn_2O_3 \leftrightarrow 4\ Mn_3O_4 + O_2 \qquad (11)$$

is chosen as the model reaction system. The TCS system is operated with air acting as both heat transfer fluid (HTF) and carrier of the gaseous reactant/product ($O_2$).

As TCS essentially presents a gas-solid chemical reactor operating in an unsteady-state regime, the proper selection and design of a specific TCS configuration should stem from the principles that have been well established by reaction-engineering practice [34,35]. According to those principles, the particle size distribution of the TCS material affects not only the gas-solid reaction kinetics but it also imposes a specific reactor type. Sub-millimeter particles with a broad size distribution are generally handled in fluidized-bed reactors because packed beds comprising such particles suffer from excessive gas channelling induced by large pressure gradients. Conversely, larger, uniformly-sized granules or pellets (>2 mm) are generally suitable for packed-bed reactors as fluidized beds tend to spout for such granules or pellets, which is undesirable for physical and chemical operations [35].

The two reactor types, fluidized and packed beds, feature different contacting patterns that, in turn, lead to different spatial and temporal temperature distributions of gas and solids. Namely, due to good mixing the temperature of the solids in a fluidized bed can be considered spatially uniform so that the gas leaves the bed at the temperature of the solids [35]. On the contrary, in a packed bed, the solids do not mix and thus their temperature varies with both time and space. The difference in the spatial temperature distributions of the solid phase in these two reactor types is reflected by the difference in the temporal outflow temperatures of the HTF, which ultimately influences the integration of the TCS into the CSP plant.

To determine the role of the reactor type in imposing the optimal TCS integration into a CSP plant, the reactors are modelled based on empirical reduction/oxidation rate laws that are adjusted for the intra-particle diffusion in the granules. Two idealized contacting patterns are assumed: (1) an axially-dispersed plug flow of gas through stationary solids for the packed bed and (2) a plug flow of gas through a well-mixed batch of solids for the fluidized bed, such that the gas leaves the bed at the temperature of the solids. The solids are assumed to have a diameter of 5 mm in the packed bed and 100 μm in the fluidized bed, respectively.

[1] Material presented in this section has been published in [33].

Figure 27 shows a comparison of the air temperatures as a function of time at the inlet and outlet of the packed- and fluidized-beds operated under quasi-steady-state conditions[2]. For both reactor types, air enters the bed at $T_{f,c,in}$ = 1273 K during a charging period of 6 hours and at $T_{f,d,in}$ = 373 K during a discharging period of 6 hours (see solid lines). The packed bed TCS is charged by feeding hot air from the top, and discharged by feeding cold air from the bottom. Because of this flow reversal, the axial temperature gradient in the solid phase can be maintained throughout the entire charging-discharging cycle and thus the granules at the bottom are not heated appreciably. Therefore, the HTF leaves the packed bed at a constant temperature of $T_{f,c,out}$ = 373 K during the entire charging period (dashed line). Different from the packed bed, the temperature of the solids in the fluidized bed is uniform due to spatial mixing. Since the HTF approaches the temperature of the solids, the HTF outflow temperatures during charging and discharging are coupled to the temperatures at which the reduction and oxidation are favorable, respectively. Therefore, the HTF leaves the fluidized bed at $T_{f,c,out} \approx$ 1180 K during most of the charging period and at $T_{f,d,out} \approx$ 1090 K during most of the discharging period. Whereas the HTF outflow temperatures of the two reactor types are similar during discharging, it is important to note that during charging the outflow temperature of the fluidized bed is significantly higher.

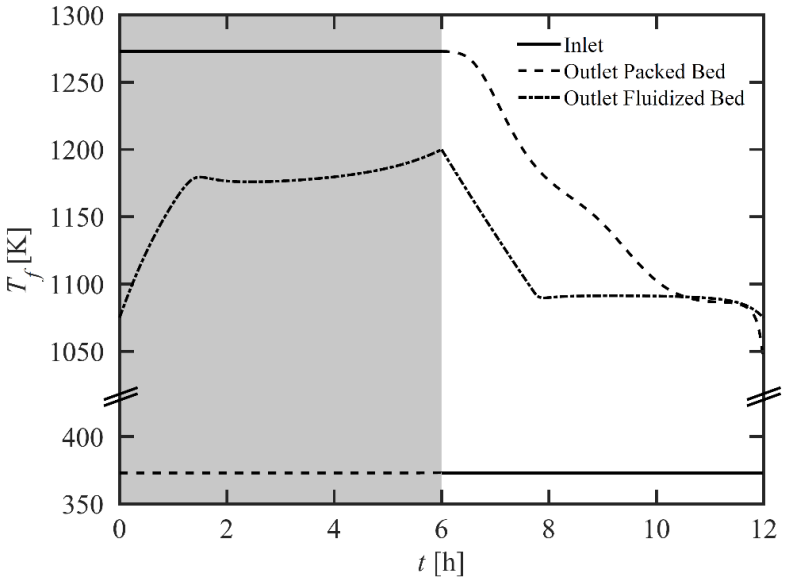


***Figure 27:*** *Comparison of air temperatures as a function of time at the inlet of the packed and fluidized beds (solid lines), the outlet of the packed bed (dashed line), and the outlet of the fluidized bed (dash-dotted line) during a charging-discharging cycle.*

The preferred integration of the TCS into the CSP plant is selected based on the computed HTF outflow temperatures and the requirements by both the power block and the solar field. The first and common way of storage integration is the parallel configuration shown in Fig.

[2] Results are considered to be in a quasi-steady state when the maximum local temperature difference between the final states of two subsequent cycles is less than 0.01 K in the gas phase.

28, in which the mass flow leaving the solar field is split into a portion flowing through the storage heat exchanger (HX) and the remainder flowing through the power-block HX. The second option is the serial configuration shown in Fig. 29, where the entire flow of the HTF leaving the solar field is passing first through the storage and then through the power-block HXs. The parallel and serial configurations must satisfy several constraints for efficient operation. During discharging, the constraints are identical: the storage should provide heat at temperatures that are sufficiently high to run the power block. For this case study, it is assumed that this constraint is fulfilled. During charging, however, the constraints are not identical. In the serial configuration, $T_{f,c,out}$ must be high enough to drive the power block. The parallel configuration requires $T_{f,c,out} \approx T_{PB,out}$ to reduce exergy losses due to mixing. These constraints, and the results presented above on the air outflow temperatures during charging, can now be seen to dictate how packed and fluidized bed reactors should be integrated into a CSP plant.

For a packed bed TCS, the chosen operating conditions allow for $T_{f,c,out} \approx T_{f,d,in} = T_{PB,out}$, thus the streams from the TCS and power-block HXs can be merged with low exergy losses. Accordingly, a parallel configuration is chosen for the packed bed. Conversely, for a fluidized bed, $T_{f,c,out}$ is coupled to the reduction temperature $T_{red}$ and therefore $T_{f,c,out} \approx T_{red} >> T_{PB,out}$. A parallel configuration would therefore lead to large exergy losses due to mixing. Accordingly, a serial configuration is chosen for the fluidized bed.

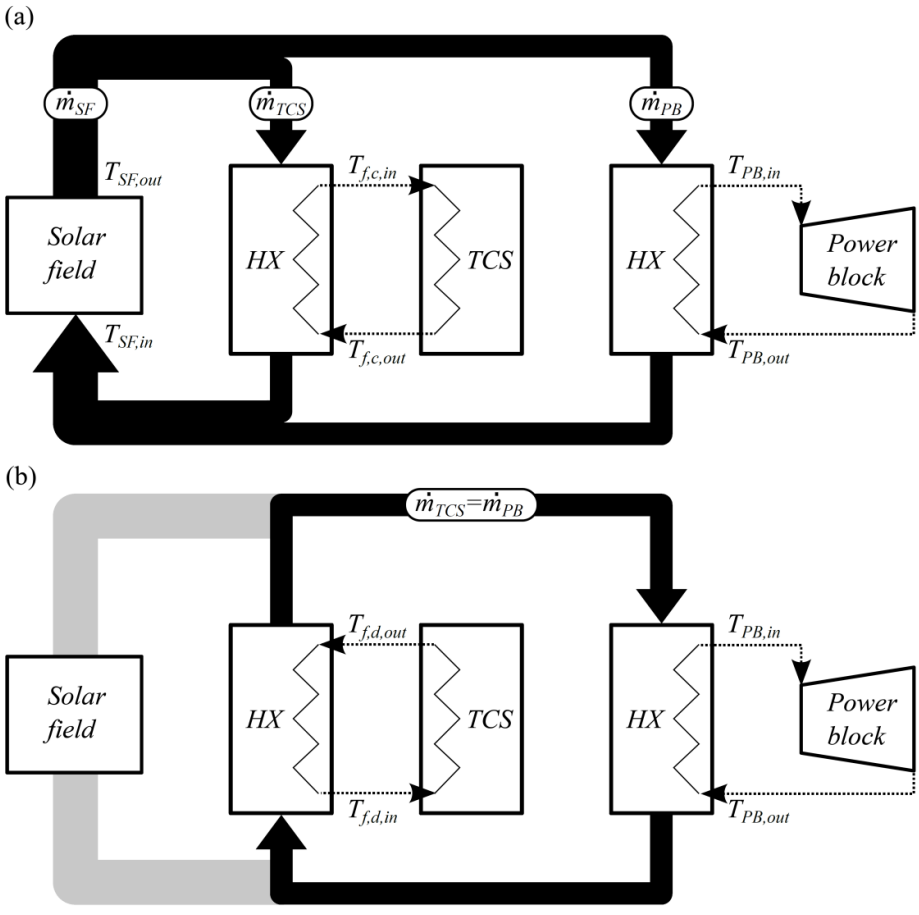


***Figure 28:*** *Schematic depiction of a parallel configuration of the TCS and the power block during (a) charging and (b) discharging.*

Having determined suitable CSP plant configurations for packed and fluidized bed TCS reactors, these configurations are now assessed using the following criteria: (1) gravimetric energy storage density, (2) HTF temperature at the power-block inlet, and (3) flexibility in adjusting the electricity production.

The gravimetric energy storage density $\bar{e}_{tot}$ relates the energy that can be stored in a TCS reactor during one charging period to the mass of storage material in the bed. The higher $\bar{e}_{tot}$, the less material is required to reach a given storage capacity and the lower the storage material costs. $\bar{e}_{tot}$ is given by the sum of the chemically stored energy $e_{chem}$, which is calculated from the change in solid conversion between the beginning and the end of charging, and the sensible heat $e_{sens}$, which is calculated from the temperature increase the solids are subjected to during the charging period. The resulting contributions of sensible and chemically stored energy in the packed and fluidized beds are compared in Table 6. It is seen that about 63 % of the total energy is stored chemically in the fluidized bed. By contrast, the chemically stored energy accounts for only about 9 % of the total stored energy in the packed bed because only about 14 % of the storage material has reacted. Nevertheless, the gravimetric energy storage density of the packed bed is approximately 11 % higher than that of the fluidized bed because of the much larger proportion of sensible heat. Thus, it is important to account for the contribution of the sensible heat when comparing TCS reactor types. It should be emphasized that these results are valid only for this specific case study because they are dependent on the reaction system and the operating conditions.

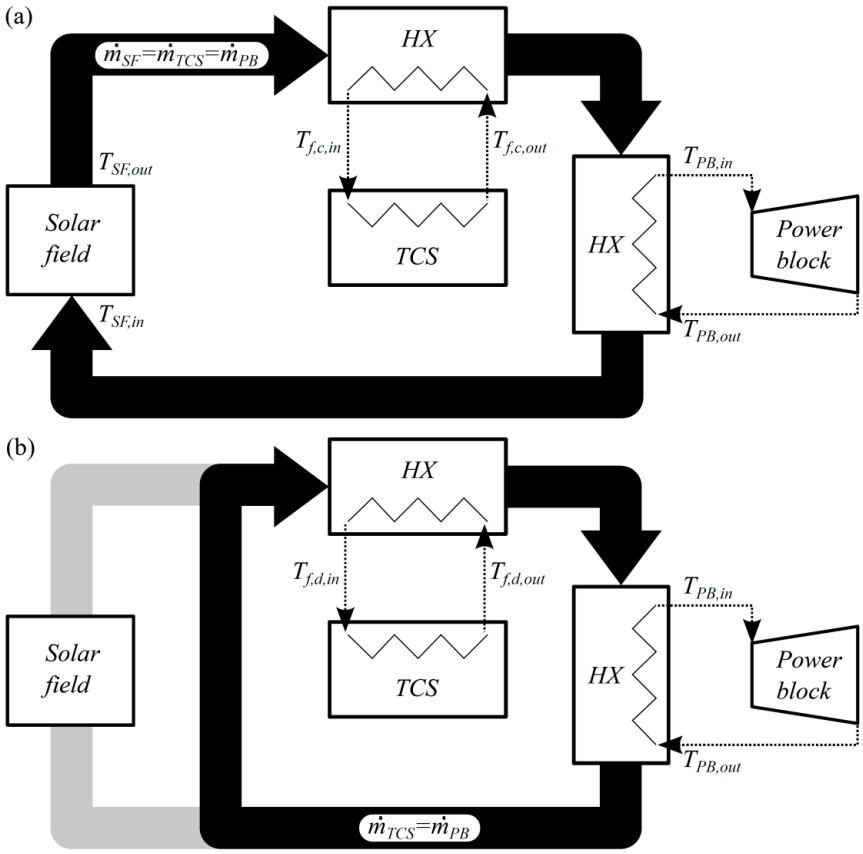


***Figure 29:*** *Schematic depiction of a serial configuration of the TCS and the power block during (a) charging and (b) discharging.*

As long as the maximum operating temperature of the power block is not exceeded, higher temperatures at the inlet of the power block are desirable. They may offer at least one of the following advantages: (1) more compact HX that couples the HTF from the solar field with the working fluid of the power block, (2) potential increase of the heat-to-electricity conversion efficiency of a given power cycle according to Carnot's principle, and/or (3) application of a different power block technology operating at higher temperatures and thereby with increased efficiencies (e.g. a Rankine cycle combined with a gas turbine) [36,37]. In the parallel configuration, thermal energy is transferred directly from the solar field to the power block during charging (see Fig. 28(a)) and therefore $T_{PB,in} = T_{SF,out} = 1273$ K. Conversely, in a serial configuration, some of the thermal energy is transferred to the TCS before entering the power block (see Fig. 29(a)) and therefore $T_{PB,in} = T_{f,c,out} < T_{f,c,in} = T_{SF,out}$ (see dash-dotted line for charging in Fig. 27). Thus, $T_{PB,in}$ is generally higher during charging for a parallel configuration than for a serial configuration. Note that in this study, the packed bed in a parallel configuration also leads to higher values of $T_{PB,in}$ during most of the discharging phase as can be seen from the outflow temperatures during discharging in Fig. 27.

**Table 6. Contribution of sensible ($e_{sens}$) and chemically stored energy ($e_{chem}$) to the gravimetric energy storage densities ($\bar{e}_{tot}$) in the packed- and fluidized beds.**

| | $e_{sens}$ [MJ/kg$_{Mn_2O_3}$] | $e_{chem}$ [MJ/kg$_{Mn_2O_3}$] | $\bar{e}_{tot}$ [MJ/kg$_{Mn_2O_3}$] |
|---|---|---|---|
| Packed bed | 0.304 (91 %) | 0.030 (9 %) | 0.334 |
| Fluidized bed | 0.111 (37 %) | 0.189 (63 %) | 0.300 |

The flexibility in adjusting the electricity production in the parallel and serial configurations has been compared in detail in [33]. For the sake of brevity, only the most important difference between the two configurations will be presented here. By appropriate sizing of the solar field and adjustment of the HTF mass flow rates in a parallel configuration, the charging rate of the TCS ($\dot{Q}_{TCS,c}$) can be set independently of the rate at which heat is transferred to the power block ($\dot{Q}_{PB,c}$). Thus, it can be ensured that sufficient heat is transferred to the TCS during charging to reach the desired duration $\tau_d$ of subsequent discharging. Conversely, in a serial configuration, the HTF transfers heat to the TCS before entering the power block. Therefore, if $T_{SF,out}$ and $T_{PB,out}$ are given by the corresponding CSP plant components, $T_{f,c,out}$ becomes the only parameter that allows the relative TCS charging rate $\dot{Q}_{TCS,c} / \dot{Q}_{PB,c}$ and thus the attainable $\tau_d$ to be adjusted. This generally leads to a trade-off in serial configurations. A decrease in $T_{f,c,out}$, achieved via variation of the reactor type, operating conditions, and/or the reaction system, leads to an increase in the attainable duration of discharging; however, it also reduces $T_{PB,in}$, thereby potentially lowering the thermal-to-electricity efficiency of the power block. A parallel configuration is not subject to this trade-off.

Based on these assessment criteria, it can be concluded that a TCS reactor should be designed such that it can be integrated with the power block in a parallel configuration. As mentioned earlier, in a parallel configuration $T_{f,c,out}$ should be kept close to $T_{PB,out}$ to minimize exergy losses. Since the reduction usually takes place at temperatures that are significantly higher than $T_{PB,out}$, the high-temperature reaction zone should be combined with a cooling zone, in which the HTF is cooled from the reduction temperature down to $T_{f,c,out} \approx T_{PB,out}$. Although the presented packed bed TCS is suitable for a parallel configuration, it converts only a fraction of the reactants (~14 %). The non-reacting portion of the reactants could thus be replaced by low-cost inert materials, leading to a combined thermochemical-sensible energy storage consisting of a high-temperature reaction TCS zone and a sensible-heat storage unit as the cooling section. Further reactor concepts that would also fulfill the requirements for integration into a parallel configuration are discussed in [33].

## List of abbreviations

| | |
|---|---|
| CNRS | Centre National de la Recherche Scientifique, France |
| CSP | Concentrating Solar Power |
| DSC | Differential Scanning Calorimetry |
| ICDD | International Centre for Diffraction Data |
| ICP-OES | Inductively Coupled Plasma with Optical Emission Spectrometer |
| IMDEA | Instituto Madrileño de Estudios Avanzados, Mósteles, Spain |
| HRSEM | High-Resolution Scanning Electron Microscopy |
| HTF | Heat Transfer Fluid |
| HX | Heat Exchanger |
| PSI | Paul Scherrer Institute, Switzerland |
| PXRD | Powder X-Ray Diffraction |
| SEM | Scanning Electron Microscopy |
| TCS | Thermochemical Storage |
| TES | Thermal Energy Storage |
| TGA | Thermogravimetric Analysis |
| XRD | X-Ray Diffraction |

## References


[1] L. André, S. Abanades, G. Flamant, Screening of thermochemical systems based on solid-gas reversible reactions for high temperature solar thermal energy storage, Renew. Sustainable Energy Rev., 2016, 64, 703-715.

[2] A.H. Abedin, M.A. Rosen, A critical review of thermochemical energy storage systems. The Open Renewable Energy Journal, 2011, 4, 42-46.

[3] A. Solé, X. Fontanet, C. Barreneche, I. Martorell, A. I. Fernández, L.F. Cabeza, Parameters to take into account when developing a new thermochemical energy storage system, Energy Procedia, 2012, 30, 380-387.

[4] A. Solé, I. Martorell, L.F. Cabeza, State of the art on gas-solid thermochemical energy storage systems and reactors for building applications, Renew. Sustain. Energy Rev., 2015, 47, 386-398.

[5] L. André, S. Abanades, L. Cassayre, High-temperature thermochemical energy storage based on redox reactions using Co-Fe and Mn-Fe mixed metal oxides, J. Solid State Chem, 2017, 253, 6-14.

[6] B. Wong, L. Brown, F. Schaube, R. Tamme, C. Sattler, Oxide based thermochemical heat storage. Presented at SolarPACES, 2010, Perpignan, France.

[7] C.W. Bale, E. Bélisle, P. Chartrand, S.A. Decterov, G. Eriksson, A.E. Gheribi, K. Hack, I.H. Jung, Y.B. Kang, J. Melançon, A.D. Pelton, S. Petersen, C. Robelin, J. Sangster, P. Spencer, M.A. Van Ende, FactSage Thermochemical Software and Databases, 2010-2016. Calphad, 2016, 54, 35-53.

[8] I.H. Jung, S.A. Decterov, A.D. Pelton, H.M. Kim, Y.B. Kang, Thermodynamic evaluation and modeling of the Fe-Co-O system, Acta Materialia, 2004, 52, 507-519.

[9] Y.B. Kang, I.H. Jung, Thermodynamic modeling of oxide phases in the Fe-Mn-O system, J. Phys. Chem. Solids, 2016, 98, 237-246.

[10] M. Neises, S. Tescari, L. De Oliveira, M. Roeb, C. Sattler, B. Wong, Solar-heated rotary kiln for thermochemical energy storage, Solar Energy, 2012, 86, 3040-3048.

[11] C. Agrafiotis, M. Roeb, M. Schmücker, C. Sattler, Exploitation of thermochemical cycles based on solid oxide redox systems for thermochemical storage of solar heat. Part 2: Redox oxide-coated porous ceramic structures as integrated thermochemical reactors/heat exchangers, Solar Energy, 2015, 114, 440-458.

[12] C. Agrafiotis, S. Tescari, M. Roeb, M. Schmücker, C. Sattler, Exploitation of thermochemical cycles based on solid oxide redox systems for thermochemical storage of solar heat. Part 3: Cobalt oxide monolithic porous structures as integrated thermochemical reactors/heat exchanger, Solar Energy, 2015, 114, 459-475.

[13] G. Karagiannakis, C. Pagkoura, A. Zygogianni, S. Lorentzou, A.G. Konstandopoulos, Monolithic ceramic redox materials for thermochemical heat storage applications in CSP plants, Energy Procedia, 2014, 49, 820-829.

[14] T. Block, N. Knoblauch, M. Schmücker, The cobalt-oxide/iron-oxide binary system for use as high temperature thermochemical energy storage material, Thermochimica Acta, 2014, 577, 25-32.

[15] M. Neises, S. Tescari, L. De Oliveira, M. Roeb, C. Sattler, B. Wong, Solar-heated rotary kiln for thermochemical energy storage, Sol. Energy, 2012, 86, 3040-3048.
[16] S. Tescari, C. Agrafiotis, S. Breuer, L. De Oliveira, M. Neises-von Puttkamer, M. Roeb, C. Sattler, Thermochemical solar energy storage via redox oxides: materials and reactor/heat exchanger concepts, Energy Procedia, 2014, 49, 1034-1043.
[17] T. Block, M. Schmücker, Metal oxides for thermochemical energy storage: a comparison of several metal oxide systems, Sol. Energy, 2016, 126, 195–207.
[18] A.J. Carillo, D.P. Serrano, P. Pizzaro, J.M. Coronado, Thermochemical heat storage based on the $Mn_2O_3/Mn_3O_4$ redox couple: influence of the initial particle size on the morphological evolution and cyclability. J Mater Chem A, 2014, 2, 19435-19443.
[19] A.J. Carillo, D.P. Serrano, P. Pizzaro, J.M. Coronado, Improving the Thermochemical Energy Storage performance of the $Mn_2O_3/Mn_3O_4$ redox couple by the incorporation of iron, ChemSusChem, 2015, 8, 1947-1954.
[20] A.J. Carillo, D.P. Serrano, P. Pizzaro, J.M. Coronado, Manganese oxide-based thermochemical energy storage: Modulating temperatures of redox cycles by Fe-Cu co-doping, J. Energy Storage, 2016, 5, 169-176. DOI:10.1016/j.est.2015.12.005.
[21] A.J. Carrillo, D.P. Serrano, P. Pizarro, J.M. Coronado, Understanding redox kinetics of iron-doped manganese oxides for high temperature thermochemical energy storage, J. Phys. Chem. C., 2016, 120, 27800-27812.
[22] F. Agnoli, B. Albouy, P. Tailhades, A. Rousset, Manganites de fer de structure spinelle déformée à très fort champ coercitif. Exemple de l'oxyde lacunaire mixte $Mn_{1.7}Fe_{1.3}O_{4+\delta}$. C.R. Acad. Sci. Paris 2, 1999, 525-530.
[23] K.J. Albrecht, G.S. Jackson, R.J. Braun, Thermodynamically consistent modeling of redox-stable perovskite oxides for thermochemical energy conversion and storage, Applied Energy, 2016, 165, 285-296.
[24] T. Masunaga, J. Izumi, N. Miura, Relationship between oxygen sorption properties and crystal structure of Fe-based oxides with double perovskite composition, Chem Eng Science, 2012, 84, 108-112.
[25] Q. Shen, Y. Zheng, C. Luo, C. Zheng, Characteristics of $SrCo_{1-x}FexO_{3-\delta}$ perovskite powders with improved $O_2/CO_2$ production performance for oxyfuel combustion, Bull Korean Chem Soc, 2014, 35, 6, 1614-1618.
[26] S.M. Babiniec, E.N. Coker, J.E. Miller, A. Ambrosini, Investigation of $La_xSr_{1-x}Co_yM_{1-y}O_{3-\delta}$ (M = Mn, Fe) perovskite materials as thermochemical energy storage media, Solar Energy, 2015, 118, 451-459.
[27] N. Galinsky, A. Mishra, J. Zhang, F. Li, $Ca_{1-x}A_xMnO_3$ (A = Sr and Ba) perovskite based oxygen carriers for chemical looping with oxygen uncoupling (CLOU), Appl Energy, 2015, 157, 358-367.
[28] S.M. Babiniec, E.N. Coker, J.E. Miller, A. Ambrosini, Doped calcium manganite for advanced high-temperature thermochemical energy storage, Int. J. Energy Res., 2016, 40, 280-284.
[29] K. Gupta, S. Singh, R.M.S. Rao, Fast, reversible $CO_2$ capture in nanostructured Brownmillerite $CaFeO_{2.5}$, Nano Energy, 2015, 11, 146-153.

[30] Z. Zhang, L. André, S. Abanades, Experimental assessment of oxygen exchange capacity and thermochemical redox cycle behavior of Ba and Sr series perovskites for solar energy storage. Solar Energy, 2016, 134, 494-502.
[31] M. Ezbiri, K.M. Allen, M. E. Gàlvez, R. Michalsky, A. Steinfeld, ChemSusChem, 2015, 8, 1966–1971.
[32] D.N. Mueller, R.A. De Souza, H.I. Yoo, M. Manfred, Chem. Mater., Correlation of the formation and the decomposition process of the BSCF perovskite at intermediate temperatures, 2012, 24, 269 −274.
[33] S. Ströhle, A. Haselbacher, Z.R. Jovanovic, A. Steinfeld, The effect of the gas-solid contacting pattern in a high-temperature thermochemical energy storage on the performance of a concentrated solar power plant, Energy Environ. Sci. 2016, 9, 4, 1375–1389. DOI: 10.1039/C5EE03204K.
[34] G.F. Froment, K. Bischoff, J. De Wilde, Chemical Reactor Analysis and Design. Wiley New York. 1990, ISBN: 0-4715-2190-6.
[35] D. Kunii, O. Levenspiel, Fluidization Engineering, Butterworth-Heinemann Boston. 1991, ISBN: 978-0-409-90233-4.
[36] N.P. Siegel, Thermal energy storage for solar power production. Wiley Interdiscip. Rev. Energy Environ., 2012, 1, 2, 119–131. DOI: 10.1002/wene.10.
[37] Z. Ma, G. Glatzmaier, M. Mehos, Fluidized bed technology for concentrating solar power with thermal energy storage. J. Sol. Energy Eng., 2014, 136, 3, 031014. DOI: 10.1115/1.4027262.